The Impact of Different Atmospheric CO_2 Concentrations on Large Scale Miocene Temperature Signatures

Akil Hossain[1], Gregor Knorr[1], Wilfried Jokat[1,2], Gerrit Lohmann[1,3], Katharina Hochmuth[4,5], Paul Gierz[1], Karsten Gohl[1] and Christian Stepanek[1]

[1] Alfred Wegener Institute, Helmholtz-Centre for Polar and Marine Research, Bremerhaven, Germany.
[2] Department of Geoscience, University of Bremen, 28359 Bremen, Germany.
[3] MARUM & Department of Environmental Physics, University of Bremen, Bremen, Germany.
[4] School of Geography, Geology and the Environment, University of Leicester, Leicester, UK.
[5] Australian Center of Excellence in Antarctic Sciences, Institute of Marine and Antarctic Studies, University of Tasmania.

Corresponding author: Akil Hossain (akil.hossain@awi.de)

Key Points:

- At a CO_2 level of 450 ppm, a Miocene simulation shows a global mean surface warming of +3.1 ^{o}C relative to the preindustrial state.
- Atmospheric CO_2 increase from 280 to 450 ppm causes a warming of ~1.4 °C, which is as strong as all other forcing factors combined.
- At higher atmospheric CO_2 levels, the Miocene climate shows a reduced polar amplification linked to a breakdown of seasonality in the Arctic.

This article has been accepted for publication and undergone full peer review but has not been through the copyediting, typesetting, pagination and proofreading process, which may lead to differences between this version and the Version of Record. Please cite this article as doi: 10.1029/2022PA004438.

Abstract

Based on inferences from proxy records the Miocene (23.03–5.33 Ma) was a time of amplified polar warmth compared to today. However, it remains a challenge to simulate a warm Miocene climate and pronounced polar warmth at reconstructed Miocene CO_2 concentrations. Using a state-of-the-art Earth-System-Model, we implement a high-resolution paleobathymetry and simulate Miocene climate at different atmospheric CO_2 concentrations. We estimate global mean surface warming of +3.1 °C relative to the preindustrial at a CO_2 level of 450 ppm. An increase of atmospheric CO_2 from 280–450 ppm provides an individual warming of ~1.4 °C, which is as strong as all other Miocene forcing contributions combined. Substantial changes in surface albedo are vital to explain Miocene surface warming. Simulated surface temperatures fit well with proxy reconstructions at low- to mid-latitudes. The high latitude cooling bias becomes less pronounced for higher CO_2. At higher CO_2 levels simulated Miocene climate shows a reduced polar amplification, linked to a breakdown of seasonality in the Arctic Ocean. A pronounced warming in boreal fall is detected for a CO_2 increase from 280–450 ppm, in comparison to weaker warming for CO_2 changes from 450–720 ppm. Moreover, a pronounced warming in winter is detected for a CO_2 increase from 450–720 ppm, in contrast to a moderate summer temperature increase, which is accompanied by a strong sea-ice concentration decline and enhanced moisture availability promotes cloud formation in summer. As a consequence planetary albedo increases and dampens the temperature response to CO_2 forcing at a warmer Miocene background climate.

1. Introduction

Proxy reconstructions show that the Miocene was a time period of global warmth. During this time, the configuration of continents, oceans and main orographies were only moderately different from those at present. With moderately higher atmospheric CO_2 and higher temperatures, the Miocene Climatic Optimum (MCO; ~16.9–14.7 Ma) has been suggested as a partial analog for the Earth's future greenhouse climate (Steinthorsdottir et al., 2021).

During the entire Miocene most proxy records reveal that atmospheric CO_2 was near or only moderately higher than preindustrial values (Beerling & Royer, 2011; Pagani, et al., 2013; Super et al., 2018; Sosdian et al., 2020; Steinthorsdottir et al., 2021). Proxy reconstructions indicate that CO_2 concentrations were in the range of 300–600 ppm during the Miocene (Foster et al., 2017; Sosdian et al., 2018). For the MCO, a similar range of 400–600 ppm has been reported (Royer, 2001; Kürschner et al., 2008; Beerling et al., 2009; Steinthorsdottir et al., 2021). However, some reconstructions suggest that CO_2 levels may have been up to 1137 ppm (Sosdian et al., 2018; Stoll et al., 2019; Rae et al., 2021; Herbert et al., 2022).

Previous modeling studies targeting the Early, Middle and Late Miocene using CO_2 concentrations of 200 to 850 ppm, modern orbital forcing, preindustrial aerosols, and taking reconstructed paleogeography, vegetation, and ice sheet differences into account, suggest a substantial high-latitude (> 60 ^{o}N and 60 ^{o}S) warming (0–18 °C in the Northern Hemisphere and 0–38 °C in the Southern Hemisphere), while the temperature increase in the tropics (~0–8 °C) is less pronounced (Herold et al., 2011a; 2011b; Knorr et al., 2011; Bradshaw et al., 2012; Herold et al., 2012; Knorr and Lohmann, 2014; Zhang et al., 2014; Stärz et al., 2017; Frigola et al., 2018; Farnsworth et al., 2019; Bradshaw et al., 2021; Burls et al., 2021). In these simulations the polar amplified warming is a robust feature and therefore the meridional temperature gradient is weaker during the Miocene than today (Knorr et al., 2011; Burls et al., 2021). The wide range of temperature increase in the Southern Hemisphere reflects differences in Antarctic Ice Sheet configurations prescribed in these simulations.

Furthermore, several modelling studies have explored the role of different potential mechanisms on the climate of the Miocene. Global temperature and climatic changes are believed to have been primarily related to increased CO_2 concentrations, paleogeographic changes (including bathymetry, orography and ocean gateways; Mikolajewicz and Crowley 1997; von der Heydt and Dijkstra, 2006; Micheels et al., 2009; Hossain et al., 2020; 2021), changes in the vegetation (Knorr et al., 2011; Bradshaw et al., 2015; Forrest et al., 2015) and the sea ice-albedo feedback mechanism. The radiative forcing including prescribed atmospheric CO_2 concentration reveals a potentially dominant control on global-scale temperature changes (Steinthorsdottir et al., 2021). Miocene non-CO_2 boundary conditions such as paleogeography and ice sheets can raise the mean global temperature by ~2 °C (Burls et al., 2021). Higher atmospheric CO_2 and more effective ocean mixing could have contributed to a reduced summer-to-winter range of temperature (Valdes et al., 1996; Spicer et al. 2004; Lohmann et al., 2022). While these mechanisms have been identified to enable warmer temperatures in the models, it is still difficult to reconcile the Miocene polar amplified warmth observed in the proxy data with simulations (Burls et al., 2021; Steinthorsdottir et al., 2021).

Comparison of MPI-ESM Middle Miocene simulations with terrestrial proxies shows best agreement with simulations of 480 and 720 ppm CO_2, whereas the best agreement for marine proxies is detected at 360 and 480 ppm CO_2 (Krapp & Jungclaus, 2011). A different study using CCSM3 Middle Miocene simulations (conducted with 335 ppm CO_2 and comparing with terrestrial temperature records) shows +1.4 °C warming in the model compared with +6 °C in the proxies (Herold et al., 2011b). Goldner et al. (2014), using CESM1.0 simulations of the Middle Miocene with 400 ppm CO_2, find that global mean surface temperature is ~4 °C colder than indicated by the proxy reconstructions. The largest cold biases are in the mid- to high-latitudes, indicating a pronounced meridional temperature gradient of ~17 °C (Herold et al., 2011b; Goldner et al., 2014; Steinthorsdottir et al., 2021). Burls et al. (2021) assess the current range of model-data agreement and current advancement toward simulating Miocene warmth and demonstrate that the degree of weakening of the meridional temperature gradient and polar amplification increases with prescribed CO_2 forcing. A recent study (Lohmann et al., 2022) reveals that, global mean surface and meridional temperature characteristics similar to those found in MCO reconstructions may be obtained in climate simulations assuming relatively moderate CO_2 levels (450 ppm) with enhanced ocean mixing. The study finds a moderate low-latitude and pronounced high-latitude warming where substantial temperature increase by up to ~5–10 °C in surface temperature is widespread and Arctic temperature anomalies reach ~12 °C relative to preindustrial (Lohmann et al., 2022). However, it remains a major challenge to successfully simulate the Miocene high-latitudes climate with a fully coupled ocean-atmosphere model (Burls et al., 2021).

Using the proxy estimates of Miocene atmospheric CO_2 levels (300–600 ppm), no climate model experiment has so far reproduced the elevated proxy paleo temperatures (Burls et al., 2021; Steinthorsdottir et al., 2021) unless the effectivity of the ocean in transporting heat between low- and high latitudes on the one hand and surface and deep ocean on the other hand is enhanced, e.g., via adaptation to the model's mixing parameterization (Lohmann et al., 2022). The model simulations cannot capture the full extent of the mid-latitude and polar warmth of the Miocene and do not have the skill to reproduce a reduced Miocene meridional temperature gradient (Goldner et al., 2014; Burls et al., 2021). It is obvious that our understanding of important physical parameters or positive feedbacks is incomplete to explain and describe processes that maintained the much weaker than preindustrial equator-to-pole temperature difference.

In this contribution we apply a state-of-the-art fully coupled Earth System Model to investigate the effect of newly and enhanced Miocene on-/offshore topographic information on the climate

sensitivity at different atmospheric CO_2 concentrations. Our model is based on the work by Sidorenko et al. (2019) but considers vegetation dynamics. The model simulation uses a high-resolution global reconstruction of Miocene bathymetry and topography (Paxman et al., 2019; Hochmuth et al., 2020a; Straume et al., 2020), which captures the major features of paleobathymetry (such as ocean ridges, plateaus and margins) and paleotopography (such as mountain ranges, e.g., the Andes). Reflecting the impact of many of these topographic features in climate simulations is only possible based on the flexibility of our ocean model with respect to spatial resolution that comes with the finite volume approach. Based on this novel setup, we investigate the climate impact of Miocene boundary conditions, separating the effect of atmospheric CO_2 and non-CO_2 Miocene boundary conditions and quantifying the most important mechanisms/feedbacks that dominate temperature responses relative to the pre-industrial climate. The model simulations are evaluated with available proxy records of terrestrial and sea surface temperature reconstructions. In our model experiments, we examine the breakdown of seasonality in the Arctic Ocean with increasing CO_2 levels.

2. Materials and Methods

Model

We apply the AWI Earth System Model, version 2.1 (AWI-ESM2.1), which consists of the atmosphere general circulation model ECHAM6 (version 6.3.05p2; Stevens et al., 2013), the land-vegetation model JSBACH (Raddatz et al., 2007; Brovkin et al., 2009; Reick et al., 2013; Giorgetta et al., 2013) and the ocean model FESOM2 (Danilov et al. 2017; Scholz et al., 2019; Sidorenko et al., 2019). The coupling between ECHAM6 and FESOM2 is achieved via the OASIS3-MCT coupler (Valcke, 2013). AWI-ESM2.1 is derived from the AWI Climate Model, version 2 (AWI-CM2) that is based on the finite-volume formulation of FESOM2 (Danilov et al. 2017; Sidorenko et al., 2019). The ECHAM6 employs a spectral dynamical core and is used in our study at T63 resolution (~1.88° x 1.88°; ~180 km horizontal resolution at the equator) with 47 vertical layers. The land surface model JSBACH runs at the same horizontal resolution as ECHAM6. Spatial resolution in the ocean on the other hand is fundamentally different as FESOM2 employs, depending on the geographical setup, either the COREII mesh (~127,000 nodes) or one of its paleo-derivates. The grid resolution for FESOM2 is high in critical areas (up to ~20 km) where small scale processes influence ocean dynamics.

AWI-ESM2.1 includes JSBACH with interactive vegetation dynamics, which ensures that climate-vegetation feedbacks are resolved in the model and that for any simulated climate state vegetation and climate are consistent with each other. Plant functional types are used in JSBACH to reduce the complexity that lies in the diversity of plants while still enabling differentiation of different plant type's characteristics in the model. Our model setup considers thirteen plant functional types that describe various types of shrubs, grasses, trees, crops, and pastures. Vegetation types compete with each other and provide distinct properties for, among others, water carrying capacity and vegetation albedo (Groner et al., 2018), thus influencing both the water and energy balance in dependence of simulated vegetation distribution. Atmosphere-ocean coupling is performed in two steps. The ocean communicates its surface state to the atmosphere and is at the same time driven by atmospheric fluxes. Four ocean fields are sent to ECHAM6: sea ice concentration, sea ice thickness, sea surface temperature (SST), and snow on sea ice. ECHAM6 computes 12 air-sea fluxes (e.g., heat, momentum, freshwater fluxes) based on surface fields provided by FESOM2. So far, the AWI-ESM2 has not only been validated under modern climate conditions (Sidorenko et al., 2019) but also has been successfully applied for marine radiocarbon concentrations (Lohmann et al., 2020), the latest

Holocene (Vorrath et al., 2020), the Last Interglacial (Otto-Bliesner et al., 2021) and the Last Glacial Maximum (Kageyama et al., 2021).

Paleobathymetry and Paleotopography

The paleomodel setup is based on the Middle Miocene time period (~14 Ma) comprising the combined high-resolution (0.1° x 0.1°) global paleobathymetry and paleotopography of Straume et al. (2020), Hochmuth et al. (2020a) and Paxman et al. (2019) (Figure 1). Paleobathymetry at latitudes south of 30°S is reconstructed following the paleobathymetric reconstruction of Hochmuth et al. (2020a), using sediment backstripping (Steckler & Watts, 1978). It is based on the reconstruction by Straume et al. (2020) and includes a suite of new paleobathymetric grids of the Southern Ocean. Hochmuth et al. (2020b) merged the Southern Ocean (Hochmuth et al., 2020a) and Antarctic bathymetry/topography (Paxman et al. 2019). This Antarctic median topography is the most recent reconstruction with a resolution of approximately 5 km. The northern part (north of 30°S) of it uses the paleobathymetric reconstruction of Straume et al. (2020). The transition between the grids is smoothed to avoid artificial abrupt changes in the bathymetry.

Straume et al. (2020) have re-evaluated the evolution of the Northern Hemisphere oceanic gateways (i.e., Fram Strait, Greenland-Scotland Ridge, Central American Seaway, and Tethys Seaway) and embedded their tectonic histories in a new global paleobathymetry and paleotopography model. The model implements updated plate kinematics, oceanic lithospheric ages, estimated sediment thickness, and paleodepths of oceanic plateaus and microcontinents.

Model setup and experimental design

In our reference Miocene simulation (MIO_450) we prescribe an atmospheric CO_2 concentration of 450 ppm. We implement a high-resolution paleobathymetry and paleotopography of the Middle Miocene as described above. The Fram Strait represents a single ocean gateway control towards the Arctic Ocean (Butt et al., 2002). The North Atlantic gateways are wide enough to maintain rotationally controlled flows across the gateways and have geometries that are documented in Table 1 (in particular, Greenland-Scotland Ridge: depth: ~410 m; Fram Strait: depth: ~2400 m, width: ~420 km). Other ocean gateways like the Canadian Archipelago, Bering Strait, Tethys Seaway and similarly the Barents Sea, evolved after the Middle Miocene. Moreover, the Panama Seaway still connects the Pacific and Atlantic Oceans. In our Miocene setup the Greenland ice sheet is absent, whereas the height of the Antarctic ice sheets and the Miocene orography (East Africa, Andes, Rocky Mountains, Tibetan Plateau) are reduced compared to preindustrial. In our simulations orbital parameters are kept constant at preindustrial values. Similarly, we prescribe aerosols and atmospheric concentrations of greenhouse gases other than CO_2 (e.g., CH_4 and N_2O) to preindustrial levels. Distribution of vegetation in all simulations is computed by the model based on vegetation dynamics in JSBACH so that geographical coverage of plants varies based upon the climatic conditions (Figure S1).

To set up the Miocene simulations we first created an ocean mesh (Figure 1b) using the paleobathymetry and paleotopography (Straume et al., 2020; Hochmuth et al., 2020a; Paxman et al., 2019). In order to create an initial spin-up of the ocean state FESOM2 was run in standalone mode for around 300 model years, initialising the ocean from a zero motion, constant temperature (3.5 ^{o}C), constant salinity (34.7 psu) state. The coupled atmosphere-ocean model was then initialized from the standalone ocean spin up and integrated for 1,000 model years until a quasi-equilibrium state had been reached (Figure S2).

For reference, we also perform another AWI-ESM2.1 model simulation using an atmospheric CO_2 concentration of 280 ppm (PI_CTRL) and employing preindustrial boundary conditions (ocean bathymetry and topography, orbital forcing and ice sheet topography), vegetation again being adjusted dynamically based on the simulated climate state. This simulation has been initialized from three-dimensional preindustrial ocean salinity and temperature fields of the Polar science center Hydrographic Climatology (Steele et al., 2001).

In order to separate effects, and analyze relative importance of CO_2 forcing versus forcing by other boundary conditions we present three additional simulations MIO_280, MIO_720 and PI_450 (Table 1). For simulation MIO_280 we apply the same CO_2 concentration as that used in PI_CTRL, but force the model with other boundary conditions as per Miocene. Simulation PI_450 adopts the same boundary conditions as PI_CTRL, while it is run with a higher CO_2 concentration of 450 ppm. In order to analyze the effect of boundary conditions, their complex interaction and synergy between them, we utilized a factor separation analysis (Stein & Alpert, 1993). Additionally, to investigate and disentangle dominant mechanisms that govern the global surface temperature changes in the high- and low-latitudes responses and shape Miocene climate, we employ both a zero-dimensional and one-dimensional energy balance model (Heinemann et al., 2009; Lunt et al., 2012). Further details of the energy balance model are given in the supplementary material (Text S1).

Results of model simulations are compared to available reconstructions of surface temperature over land and ocean. We employ Middle Miocene terrestrial annual mean temperature estimates as collected and employed in MioMIP1 (Burls et al., 2021). We compare these estimates, that are derived mainly from fossil plant data, to the annual-mean land surface temperature of our simulations. In order to quantify the agreement of simulated and reconstructed Miocene SST we rely on temperature estimates as collected in MioMIP1 (Burls et al., 2021) and as present from the Miocene temperature portal (Lawrence et al., 2021 and references therein). SST reconstructions employed in MioMIP1 are based on Mg/Ca, U^k_{37}, and TEX_{86} proxies, uncertainties are 3–5 ºC. Reconstructions of SST are representative of the Late Miocene (ranging between 11.6 and 5.33 Ma), Middle Miocene (ranging between 15.97 and 11.63 Ma) and MCO (ranging between 16.75 and 14.5 Ma). Information on all SST proxy records of Middle Miocene, MCO and Late Miocene considered in our study are, together with the original reference, provided in Table S4 and S5 (extended version of the original table published in Burls et al. (2021)).

3. Results

3.1 Climatic effect of Miocene boundary conditions

In experiment MIO_450 with Miocene boundary conditions, we simulate a mean surface air temperature of ~16.4 °C, which is warmer (~3.0 °C) than the preindustrial climate (PI_CTRL, ~13.4 °C). In comparison to the preindustrial the simulated Miocene climate shows reduced sea-ice cover and increased water vapour (Figure 2 and Table 2). Spatial temperature anomaly patterns between MIO_450 and PI_CTRL are heterogeneous (Figure 2a). In combination with ice-albedo feedback (Figure 2b and 2c), the resulting temperature variation is largely pronounced in the high-latitudes.

The most pronounced warming occurs over Antarctica, exceeding temperature anomalies of +35 °C, and Greenland (+28 °C). Other regions of exceptional warming are the Weddell Sea and Ross Sea, with a warming of up to +20 °C. Furthermore, the warming at the western border of North and South America and across the Tibetan Plateau is mainly related to topography changes between Miocene and preindustrial simulation setups (Figure 2). The only region with

a pronounced cooling is located in the Nordic Seas (~14 °C), which is associated with a relatively shallow Greenland-Scotland Ridge in comparison to preindustrial (please see section 3.2 for further details) and in combination with ice-albedo feedback (Figure 2b and 2c). Albedo changes at the continental boundaries are mostly controlled by displacement of the continents during the Miocene (Figure 1), contributing to the temperature changes in those regions (Figure 2).

3.2 Impact of atmospheric CO_2 and synergetic effects

To evaluate the relative importance of CO_2 concentrations (ΔCO_2) and non-CO_2 Miocene boundary conditions (ΔBC) as forcing factors we used a factor separation analysis (Stein & Alpert, 1993). We compare our simulations PI_450 and MIO_280 with the preindustrial climate simulation (PI_CTRL). According to this analysis, the synergy ($\Delta Synergy$) is the difference of the combined boundary conditions effect ($\Delta(BC+CO_2)$) and the singular effects ΔBC and ΔCO_2 (Figure 3). The two simulations PI_450 and MIO_280 (Figure 3a and 3b) clearly show that changes in the CO_2 concentrations and non-CO_2 boundary conditions strongly alter the global temperature pattern. The global-mean surface temperature increase of ~3.1 °C in MIO_450 can be attributed to the impact of the atmospheric CO_2 increase from 280 to 450 ppm (ΔCO_2 = +1.4 °C) and the effect of boundary conditions changes other than CO_2 (ΔBC = +1.4 °C), while the synergy between them is positive ($\Delta Synergy$ = +0.3 °C).

The resulting temperature increase is very pronounced over Antarctica (+30 °C), Greenland (+22 °C), Weddell Sea and Ross Sea, which is largely controlled by reduced ice sheet height and sea ice cover during the Miocene. In contrast, a pronounced cooling occurs in the Nordic Seas and Barents Sea where temperature decreased down to −16 °C in combination with increased sea ice cover and surface albedo (Figure 2). Temperature changes in this region are related to a Greenland-Scotland Ridge that is shallower than for the preindustrial (Hossain et al., 2020). The relatively shallow Greenland-Scotland Ridge reduces the transport of warmer and saltier Atlantic waters to the Nordic Seas. The reduced exchange of warm salty water across the gateway largely controls the overall temperature and salinity decrease (by up to −6 psu) at the ocean surface in the Nordic Seas and Barents Sea (Figure S3; Hossain et al., 2020).

The factor separation analysis indicates that warming over the Arctic and Southern Ocean (except for the regions of the Weddell Sea) can be attributed rather equally to both forcing factors (atmospheric CO_2 and non-CO_2 Miocene boundary conditions). The warming at the western border of North America, southern border of Siberia and Tibetan Plateau is related to displacement of the continents (between Miocene and preindustrial; Figure 3a), while the warming over all land masses is due to CO_2 changes (Figure 3b). The surface temperature changes in the Nordic Seas and Barents Sea are dominated by the associated bathymetry changes in these regions that predominantly have a cooling effect on climate.

The Labrador Sea and the North Atlantic (e.g., south of Iceland) are strongly influenced by the positive (i.e., warming) synergy between the non-CO_2 boundary conditions and the CO_2 forcing. In contrast to these regions the negative (i.e., cooling) synergy is pronounced over Nordic Seas and Barents Sea. At the southern high-latitudes, the negative synergy effect is pronounced in the Southern Ocean, particularly in the Weddell Sea, the Ross Sea and larger coastal region of the Antarctica (Figure 3c). The enhanced synergy impact in these regions can be explained by high temperature sensitivity of sea-ice and associated feedbacks that are already triggered by global temperature change in ΔBC and ΔCO_2. Therefore, the combined effect of both forcing factors can cause a weaker warming at regional-scale, as well as an overall positive effect at the global-scale (Figure 3d).

To investigate the dominant mechanisms that govern global surface temperature differences in the high- and low-latitudes responses, we analyse a one-dimensional energy balance model for surface air temperature (SAT), which shows a good agreement with the global mean SAT of the earth system model (Table S1). Deviations between the SAT as diagnosed by the one-dimensional energy balance model and the simulated climate are mainly occurring in the high latitudes (Figure 4a). The increase in zonal mean SATs, that comes with Miocene boundary conditions and increased CO_2 and that is biased towards the high latitudes, is associated with increased water vapor in the atmosphere, which reduces effective longwave emissivity (Figure 4b, c).

Our study suggests that substantial changes in surface albedo (Figure 4c) are vital to explain the Miocene surface warming (Figure 2). We compare the effective longwave emissivity and the planetary albedo of MIO_450 and PI_CTRL to quantify the impact on surface warming and to better explain the global radiation balance. The planetary albedo in MIO_450 is reduced by ~0.01 (relative to PI_CTRL; 0.30), which causes less shortwave reflection, and, as a result, warming. The emissivity in MIO_450 also decreases by ~0.02, which is largely governed by a ~19% increase of the water vapour content in the atmosphere (Table 2) and enhances the greenhouse effect. Based on the energy balance model (Heinemann et al., 2009; Lunt et al., 2012) the impact of albedo and emissivity can be quantified (see for example Lohmann et al., 2022). About two-thirds (~1.74 K) of the overall temperature anomaly with respect to PI_CTRL (~2.60 K) are due to emissivity, whereas the remainder is due to reduced planetary albedo (Figure 4 and Table S1).

3.3 Data-model comparison

We compare the simulated annual-mean surface temperatures of land and ocean for Miocene experiments against available proxy data estimates of Middle Miocene, MCO and Late Miocene temperature proxy reconstructions (for details of the proxy compilation please see Table S4 and S5 in the supplementary material; Burls et al., 2021; Lawrence et al., 2021 and references therein). Reconstructed temperatures are compared to zonal means of simulations in Figure 5. Spatial patterns of simulated surface temperatures are shown in Figure 6 alongside a dataset of Middle Miocene temperature proxy reconstructions (Burls et al., 2021; Lawrence et al., 2021). Both the terrestrial and SST proxies of Middle Miocene indicate a reduced meridional temperature gradient while the model simulates a substantial meridional temperature gradient (Figure 5a and 5b). The model simulations appear to demonstrate a reasonable fit with the low-latitude Middle Miocene SST records and the mid-latitude Middle Miocene SAT records (Figures 5b and 6). Simulations generally suffer from cold biases outside of the tropics. Modelled mid- to high-latitude warmth tends to show better agreement with the proxy data as CO_2 concentrations increase.

We detect cold SST biases in the Southern Ocean and the North Atlantic (Figure 6). In general, model simulations capture low to mid-latitude temperature distribution of the proxy data, but fail to capture the full extent of Miocene polar amplified warmth observed in the proxy records (Figure 5a and 5b). The nature of this mismatch can be explained by observing the equator-to-pole temperature gradient that is 4.9 to 9.9 °C larger in the simulations than in the proxy reconstructions (Table 2). A reduction in meridional temperature gradient is detected as CO_2 concentrations increase. Our simulations, MIO_450 and MIO_720 are roughly 5.8±0.8 °C and 4.5±0.8 °C colder compared to the SST calculated from the proxy records presented here (~24.5±0.8 °C; Burls et al., 2021). However, the model simulations show general agreement and a high and significant correlation coefficient with proxy data. The most significant correlation coefficient and lowest root-mean-square error (RMSE) with SST records is detected for the Miocene simulation with 720 ppm of CO_2 (R = 0.86, RMSE = 7.1; Figure 7; Table S2).

However, correlation coefficients of other simulations are very similar. Terrestrial temperature proxies also demonstrate the lowest RMSE with the MIO_720 simulation.

Deviation between model and reconstructions becomes larger when we consider the MCO SST proxies (Figure 5; Table S2). Our model simulations struggle to reproduce the elevated temperatures and reduced meridional temperature gradient estimated by the MCO SST proxies. In our experiments, the low-latitudes appear to provide a reasonable fit with Late Miocene proxies while mid- to high-latitudes are too cold (Figures 5 and S4). We find most significant correlation coefficient and lowest deviations for the simulation with 720 ppm of CO_2 (R = 0.90, RMSE = 4.3; Table S2). Overall, we find that model simulations have better alignment with Late Miocene proxies than with reconstructions of Middle Miocene and MCO (Figures 7 and S5) We note that the overall disagreement of simulated and reconstructed climate (i.e., a relatively cold climate state in the model) is evident in different regions, and in particular at the high latitudes (Figures 5 and 6). Furthermore, we remark that, despite the relatively long model integration, the overall energy balance of the Earth System is not yet in equilibrium, with the net energy flux into the Earth System being positive and increasing with the prescribed level of carbon dioxide (Table S1). We suggest that prolonged integration of the model could reduce the model data mismatch in particular in those regions where (polar) amplification of global warming is large (Figures 5 and 8), which have an overlap with regions of substantial model data mismatch.

3.4 Meridional temperature changes at elevated CO_2 concentration

Across the Miocene simulations (at different atmospheric CO_2 concentrations) the magnitude of high-latitude warming spans 10.2–13.3 ^{o}C in the Southern Hemisphere and 1.7–11.8 ^{o}C in the Northern Hemisphere compared to preindustrial, while low-latitude warming spans 0.6–3.4 ^{o}C (Figure 8). We observe substantial polar amplified warmth in the high latitudes of both hemispheres across all Miocene simulations. In the higher northern latitudes, there is a pronounced polar amplification effect for CO_2 increase from 280 to 450 ppm (latitudinal mean surface temperature increase of ~5.4 ^{o}C; latitudes >80 ^{o}N). The effect is weaker for the same radiative CO_2 forcing change from 450 to 720 ppm (latitudinal mean surface temperature increase of ~4.7 ^{o}C; latitudes >80 ^{o}N) (Figure 8a). That means the impact of the CO_2 forcing is less pronounced at higher levels of CO_2 forcing. Temperature difference at low latitudes, is almost constant independent of the background level of CO_2.

Our warmest Miocene climate state with a CO_2 level of 720 ppm is characterized by a breakdown of seasonality in the Arctic Ocean. We detect a pronounced warming in boreal winter (December-January-February; DJF mean surface temperature increase of ~10.9 ^{o}C) for a CO_2 increase from 450 to 720 ppm, in contrast to a moderate boreal summer (June-July-August; JJA) temperature increase (mean surface temperature increase of ~1.0 ^{o}C; Figure 8 and Table 2). The change in the boreal summer temperature signature is accompanied by a strong sea-ice concentration decline (Figures 8 and S6) and enhanced moisture availability promotes high-level cloud formation in the summer months (Figures 9 and S7-S8). As a consequence of the enhanced cloud formation in the boreal summer months, the planetary albedo increases (Figure S9) which enhances the reflection of solar radiation. It dampens the temperature response to the CO_2 forcing at a warmer Miocene background climate. In contrast, decreased sea ice extent and turbulent surface heat fluxes increase humidity in the lower atmosphere during boreal winter, which increases the low-level cloud cover (Figure S10). During polar night, this enhances downward longwave radiation, leading to a positive cloud-sea ice feedback. The heat released by the ocean and the cloud-sea ice feedback induce a pronounced warming in boreal winter (~22.2 ^{o}C, relative to preindustrial; Table 2; Figures 9 and S8). In addition, we detect a pronounced Arctic warming in boreal fall (September-

October-November; SON) for a CO_2 increase from 280 to 450 ppm (mean surface temperature increase of ~8.9 ºC), in comparison to a weaker temperature increase for a CO_2 change from 450 to 720 ppm (mean surface temperature increase of ~3.2 ºC; Figure 8f and Table 2). The heat released by the ocean and the cloud feedbacks (high-level cloud cover is reduced, low-level cloud cover is increased) induce a pronounced warming in boreal fall for a CO_2 increase from 280 to 450 ppm (Table 2; Figures 9, S7 and S10). The dampening of Arctic amplification to the CO_2 forcing for a CO_2 change from 450 to 720 ppm is accompanied by a strong sea-ice concentration decline (Figure 8j) and associated with surface albedo decrease (0.38 to 0.12; Figure S11) and a moderate high-level cloud cover reduction (Figures S7 and S10). Finally, we detect a similar moderate Arctic warming in boreal spring (March-April-May; MAM) for the same radiative CO_2 forcing changes from 280 to 450 ppm (mean surface warming of ~4.6 ºC) and 450 to 720 ppm (~4.3 ºC; Figure 8d).

4. Discussion

Findings derived from our climate simulations (Table 2) suggest a global annual average warming similar to previously published Middle Miocene climate simulations by Krapp & Jungclaus (2011), who found a global mean SAT of 17.1–19.2 ºC (at a CO_2 level of 480–720 ppm. Our simulated Miocene climate (based on CO_2 concentrations in the range of 280–720 ppm) shows a global mean SST of 17.5–20.0 °C which is in good agreement with the Early to Middle Miocene simulations studied by Burls et al. (2021), but colder (3.7–6.7 °C) than the global mean surface temperature estimates for the Middle Miocene (24.46°C ± 0.81°C) based on the compiled proxy SST synthesis (Burls et al., 2021). The modelled Miocene climate (MIO_450) exhibits a sensitive SAT response (+1.4 °C) to CO_2 increase, which is governed by various climate feedbacks, such as water vapour (Soden & Held, 2006; +19% increase compared to preindustrial; Table 2) and sea-ice changes (Figure S6; Soden & Held, 2006; Knorr et al., 2011).

Non-CO_2 Miocene boundary conditions employed by us (including paleobathymetry and ice sheet height) raise global temperature by +1.4 °C in agreement with previous estimates (Burls et al., 2021). Strong regional warming is detected in response to reduced height of the Antarctic ice sheet and absence of a Greenland ice sheet but the influence is limited beyond the both hemispheres high latitudes (Burls et al., 2021). The largest contributor of warming relative to preindustrial (Figure 5) is caused by atmospheric CO_2 and land surface characteristics changes (e.g., surface albedo) that are linked with aspects of the global energy balance (e.g., effective longwave emissivity, planetary albedo; Figure 4; Knorr et al., 2011; Burls et al., 2021). Our climate simulations found a sea surface cooling in the Nordic Seas that is likely related to a relatively shallow Greenland-Scotland Ridge and in combination with the associated ice-albedo feedback, which is in agreement with the findings by Hossain et al. (2020).

During the MCO, different proxy reconstructions suggest that SSTs were 8–10 °C warmer than preindustrial at high-latitudes of the Southern Hemisphere (Shevenell et al., 2004), 10–15 °C warmer in the Northern Hemisphere (Super et al., 2020) and ~5–8 °C warmer in the deep ocean (Lear et al., 2015), leading to a global mean surface warming of ~7.6±2.3 °C compared to preindustrial (Goldner et al., 2014). Results of our Miocene simulations are in agreement with this reconstructed range of temperature. The equator-to-pole is 4.9–9.9 °C warmer in our simulations than that derived from proxy data (~17 °C; Goldner et al., 2014). However, our Miocene climate simulations demonstrate a reasonable fit with low-latitude Middle Miocene SST and mid-latitude Middle Miocene SAT records. In general, the model simulations capture low- to mid-latitude temperature distributions of the proxy data. Both Middle Miocene terrestrial and sea surface temperature proxies indicate a reduced meridional temperature

gradient while the model simulates a weakened, but in relation to reconstructions still pronounced meridional temperature gradient. The degree of weakening of the meridional temperature gradient and polar amplified warming increases in the simulations with prescribed CO_2 levels, but generally fails to capture the full extent of weakening of the reconstructed meridional gradient observed in the proxies, a finding supported by a previous study of Burls et al. (2021). It is noteworthy that our model simulations are not fully equilibrated, which leading the possibility that a part of the model data mismatch might be alleviated by further integration of the model (see section 3.3). Additionally, the results of high-resolution climate simulations for the Eocene time period, which utilized enhanced paleobathymetry as we did in the Southern Ocean, has improved the ability of a climate model to simulate heat transport and circulation patterns of the Southern Ocean (Sauermilch et al., 2021).

The Miocene climate simulated by us is subject to weaker polar amplification at high northern latitudes (by 0.7 ^{o}C) for CO_2 increase from 450 to 720 ppm relative to a similar change in radiative CO_2 forcing from 280 to 450 ppm (Figure 8). In polar regions, many feedback parameters are highly dependent on the presence of water in different phases and on the state of the system close to the freezing point (Goosse et al., 2018). Phase changes play a critical role in clouds of the polar region, leading to strong non-linearities in the cloud feedback (Mitchell et al., 1989; Zelinka et al., 2012). Moreover, as temperature increases, the surface area covered by ice or snow decreases at high-latitudes and the feedback strength is lowered (Goosse et al., 2018). Therefore, surface warming tends to be non-linear (deviation from the logarithmic curve) as CO_2 levels increase (Lunt et al., 2021), which supports our results.

Seasonal paleoclimate data suggest that polar amplification has a large seasonal cycle (Utescher & Mosbrugger, 2007; Goosse et al., 2018). The mean warming is at a minimum during boreal summer and maximum during boreal winter/fall with a peak in November in the Arctic Ocean (Utescher & Mosbrugger, 2007; Laîné et al., 2016). This result is again reproduced in our analysis of Miocene climate simulations. In a warmer climate, cloud cover increases (Figure S10), which increases the planetary albedo as well as the amount of reflected solar radiation. This process chain acts as a negative cloud optical depth feedback (Goosse et al., 2018). On the other hand, declining sea ice concentration during polar night (Figure 8) results in greater low-level clouds (Figure S10) and enhanced downwelling longwave radiation, leading to a positive cloud feedback. In boreal winter/fall, heat released by the ocean and cloud feedbacks induce a pronounced warming (Figures 8-9 and S8; Laîné et al., 2016; Goosse et al., 2018).

The inability of our model to capture the full extent of the reduction of meridional temperature gradient and polar amplified warmth reflected in proxies is an issue that is not only unique to either our model or to climate simulations of the Miocene epoch, but also seen in different paleoclimate modelling studies spanning the Cenozoic (Huber & Caballero, 2011; Krapp & Jungclaus, 2011; Goldner et al., 2014; Haywood et al., 2020; Steinthorsdottir et al., 2021; Burls et al., 2021). It is likely that our interpretation or understanding of proxy data signals is limited (Ho & Laepple, 2016) and our knowledge of important physical parameters or positive feedbacks is missing or incomplete to explain how climatic processes and trends are related to reconstructed temperature changes. However, implementation of enhanced ocean mixing (Lohmann at al., 2022), state-of-the-art parameterizations of cloud-aerosol interactions (Kiehl and Shields, 2013; Feng et al., 2019; Zhu et al., 2019; Zhu & Poulsen, 2019; Lunt et al., 2021) and improved representation of tidal mixing (Green & Huber, 2013; Lohmann, 2020) might improve the ability of models to simulate Miocene warmth and to reduce disagreement between modelled and reconstructed meridional temperature gradients in models and geologic records. Model simulations with elevated CO_2 concentration (up to 1100 ppm) as recently reconstructed

for the Early-Middle Miocene including the MCO by Herbert et al., (2022), might also provide a better fit between climate simulations and reconstructed temperatures.

5. Conclusions

By means of the state-of-the-art climate model AWI-ESM2.1, we have simulated Miocene climate states at different atmospheric CO_2 concentrations and evaluated the effect of model boundary conditions during the Middle Miocene. We estimate a global mean surface warming of +3.1 ^{o}C relative to the preindustrial state at a CO_2 level of 450 ppm. The atmospheric CO_2 increase from 280 to 450 ppm provides an individual warming contribution of ~1.4 °C, which is as strong as all non-CO_2 Miocene forcing contributions combined (~1.4 °C). In combination with ice-albedo feedbacks, the resulting temperature change is largely pronounced at high-latitudes. A substantial cooling appears in the Nordic Seas which is associated with a relatively shallow Greenland-Scotland Ridge in comparison to modern bathymetry and in combination with ice-albedo changes. Our simulated surface temperatures fit well with proxy reconstructions except in the high-latitudes. Incomplete model equilibration may provide a partial explanation for this finding. The high-latitude cooling bias is least pronounced in our simulation with a CO_2 concentration of 720 ppm. The most significant correlation coefficient and lowest RMSE with terrestrial and SST records are detected for the simulation with the highest CO_2 level. Our climate simulation with a CO_2 level of 720 ppm shows reduced polar amplification, since the warmest Miocene climate state is characterized by a breakdown of seasonality in the Arctic Ocean. We detect a pronounced warming in boreal fall for a CO_2 increase from 280 to 450 ppm, in comparison to a weaker warming for the same radiative CO_2 forcing changes from 450 to 720 ppm. This dampening of temperature response to the CO_2 forcing is associated with a strong sea-ice concentration decline, surface albedo decrease and moderate high-level cloud cover reduction. Moreover, a pronounced warming in boreal winter is detected for for the simulations with higher CO_2 levels, which is in contrast to a moderate boreal summer warming response. The change in the seasonal temperature response is accompanied by a strong sea-ice concentration decline. Enhanced moisture availability promotes cloud formation during the summer months. As a consequence, planetary albedo increases (i.e., the reflection of solar radiation is enhanced) and dampens the temperature response to the CO_2 forcing in a warmer Miocene background climate.

Overall, our model simulations show general agreement and a significant correlation coefficient with proxy data and are in the range of other published Early to Middle Miocene simulations. Future sensitivity studies can use our model setup and evaluate the effect of high-resolution global paleobathymetry (implemented in our study) in combination with plausible mechanisms, that have been suggested to reduce model-reconstruction mismatches, on ocean circulation and climate. Promising candidates, that might be required for providing more realistic climatic response for the Miocene, are sensitivity studies with enhanced vertical mixing in the ocean (Lohmann at al., 2022), state-of-the-art parameterizations of cloud-aerosol interactions (Lunt et al., 2021; Zhu et al., 2019; Zhu & Poulsen, 2019), changes in aerosols (Lunt et al., 2021), as well as improved representation of tidal mixing (Green & Huber, 2013; Lohmann, 2020).

Acknowledgments

This study is supported through institutional funds of the Alfred Wegener Institute (AWI) – Helmholtz Centre for Polar and Marine Research through Work Packages 3.2 (Earth system on tectonic time scales: From greenhouse to icehouse world) and the topic “Ocean and Cryosphere under climate change” of its research program PACES-II “Changing Earth – Sustaining our Future” and the joint program ‘Changing Earth - Sustaining our Future’ (PoF IV) program of

the AWI. All simulations were performed at the AWI Computing Center. Thanks go to the scientific community in DeepMIP and MioMIP for their efforts toward provision of robust paleogeography and model forcing.

Open Research

Data Availability Statement

Data from this study is available for further use through PANGAEA (Hossain et al., 2022).

Code availability: The standard source code of the FESOM2 (Finite Element Sea ice-Ocean Model) is available to the public via GitHub (https://github.com/FESOM/fesom2/). The ECHAM6 model is available upon request from the Max Planck Institute (MPI) for Meteorology in Hamburg (sebastian.rast@mpimet.mpg.de).

Competing interests: The authors declare no conflict of interest.

Reference

Beerling, D. J., Fox, A., & Anderson, C. W. (2009). Quantitative uncertainty analyses of ancient atmospheric CO2 estimates from fossil leaves. American Journal of Science, 309, 775–787. https://doi.org/10.2475/09.2009.01

Beerling, D. J., & Royer, D. L. (2011). Convergent Cenozoic CO_2 history. *Nature Geoscience*, *4*(7), 418-420. https://doi.org/10.1038/ngeo1186

Bradshaw, C. D., Lunt, D., Flecker, R., Salzmann, U., Pound, M., Haywood, A., & Eronen, J. (2012). The relative roles of CO2 and palaeogeography in determining late Miocene climate: Results from a terrestrial model-data comparison. Climate of the Past, 8(2), 715–786. https://doi.org/10.5194/cp-8-1257-2012

Bradshaw, C. D., Lunt, D. J., Flecker, R., & Davies-Barnard, T. (2015). Disentangling the roles of late Miocene paleogeography and vegetation– implications for climate sensitivity. Palaeogeography Palaeoclimatology Palaeoecology, 417, 17–34. https://doi.org/10.1016/j.palaeo.2014.10.003

Bradshaw, C. D., Langebroek, P. M., Lear, C. H., Lunt, D. J., Coxall, H. K., Sosdian, S. M., & de Boer, A. M. (2021). Hydrological impact of Middle Miocene Antarctic ice-free areas coupled to deep ocean temperatures. *Nature Geoscience*, *14*(6), 429-436.

Burls, N.J., Bradshaw, C.D., De Boer, A.M., Herold, N., Huber, M., Pound, M., et al. (2021). Simulating Miocene warmth: insights from an opportunistic Multi-Model ensemble (MioMIP1). *Paleoceanography and Paleoclimatology*, p.e2020PA004054.

Butt, F. A., Drange, H., Elverhøi, A., Otterå, O. H., & Solheim, A. (2002). Modelling Late Cenozoic isostatic elevation changes in the Barents Sea and their implications for oceanic and climatic regimes: Preliminary results. Quaternary Science Reviews, 21(14–15), 1643–1660. https://doi.org/10.1016/S0277-3791(02)00018-5

Danilov, S., Sidorenko, D. Wang, Q., & Jung, T. (2017). The Finite-volumE Sea ice–Ocean Model (FESOM2). *Geoscientific Model Development*, *10*, pp.765-789.

Farnsworth, A., Lunt, D. J., O'Brien, C. L., Foster, G. L., Inglis, G. N., Markwick, P., et al. (2019). Climate sensitivity on geological timescales controlled by nonlinear feedbacks and ocean circulation. Geophysical Research Letters, 46(16), 9880-9889.

Feng, R., Otto-Bliesner, B. L., Xu, Y., Brady, E., Fletcher, T., & Ballantyne, A. (2019). Contributions of aerosol-cloud interactions to mid-Piacenzian seasonally sea ice-free Arctic Ocean. Geophysical Research Letters, 46(16), 9920-9929.

Forrest, M., Eronen, J. T., Utescher, T., Knorr, G., Stepanek, C., Lohmann, G. and T. Hickler (2015). Climate-vegetation modelling and fossil plant data suggest low atmospheric CO_2 in the late Miocene, Clim. Past, 11, 1701-1732, doi:10.5194/cp-11-1701-2015.

Frigola, A., Prange, M., & Schulz, M. (2018). Boundary conditions for the middle Miocene climate transition (MMCT v1.0). Geoscientific Model Development, 11(4), 1607–1626.

https://doi.org/10.5194/gmd-11-1607-2018
Goldner, A., Herold, N., & Huber, M. (2014). The challenge of simulating the warmth of the mid-Miocene climatic optimum in CESM1. Climate of the Past, 10(2), 523–536. https://doi.org/10.5194/cp-10-523-2014
Goosse, H., Kay, J.E., Armour, K.C., Bodas-Salcedo, A., Chepfer, H., Docquier, D., et al. (2018). Quantifying climate feedbacks in polar regions. *Nature communications*, *9*(1), 1-13.
Green, J. A. M., & Huber, M. (2013). Tidal dissipation in the early Eocene and implications for ocean mixing. *Geophysical Research Letters*, *40*(11), 2707-2713. https://doi.org/10.1002/grl.50510
Haywood, A. M., Tindall, J. C., Dowsett, H. J., Dolan, A. M., Foley, K. M., Hunter, S. J., et al. (2020). A return to large-scale features of Pliocene climate: The Pliocene Model Intercomparison Project Phase 2. Climate of the Past Discussions. 16, 2095–2123. https://doi.org/10.5194/cp-2019-145
Heinemann, M., Jungclaus, J. H., & Marotzke, J. (2009). Warm Paleocene/Eocene climate as simulated in ECHAM5/MPIOM. Climate of the Past, 5, 785–802. https://doi.org/10.5194/cp-5-785-2009
Herold, N., Huber, M., Greenwood, D. R., Müller, R. D., & Seton, M. (2011a). Early to middle Miocene monsoon climate in Australia. Geology, 39, 3–6. https://doi.org/10.1130/G31208.1
Herold, N., Huber, M., & Müller, R. D. (2011b). Modeling the Miocene Climatic optimum. Part I: Land and atmosphere. Journal of Climate, 24, 6353–6372. https://doi.org/10.1175/2011JCLI4035.1
Herold, N., Huber, M., Müller, R. D., & Seton, M. (2012). Modeling the Miocene climatic optimum: Ocean circulation. Paleoceanography, 27, PA1209. https://doi.org/10.1029/2010PA002041
Hochmuth, K., Gohl, K., Leitchenkov, G., Sauermilch, I., Whittaker, J.M., Uenzelmann-Neben, et al. (2020a). The Evolving Paleobathymetry of the Circum-Antarctic Southern Ocean Since 34 Ma: A Key to Understanding Past Cryosphere-Ocean Developments. *Geochemistry, Geophysics, Geosystems*, *21*(8), e2020GC009122.
Hochmuth, K., Paxman, G. J. G., Gohl, K., Jamieson, S. S. R., Leitchenkov, G. L., Bentley, M. J., et al. (2020b). Combined palaeotopography and palaeobathymetry of the Antarctic continent and the Southern Ocean since 34 Ma. PANGAEA, https://doi.pangaea.de/10.1594/PANGAEA.923109
Hossain, A., Knorr, G., Lohmann, G., Stärz, M., & Jokat, W. (2020). Simulated Thermohaline Fingerprints in Response to Different Greenland-Scotland Ridge and Fram Strait Subsidence Histories. Paleoceanography and Paleoclimatology: e2019PA003842. https://doi.org/10.1029/2019PA003842
Hossain, A., Knorr, G., Jokat, W., & Lohmann, G. (2021). Opening of the Fram Strait led to the establishment of a modern-like three-layer stratification in the Arctic Ocean during the Miocene. *Arktos*, 1-12. https://doi.org/10.1007/s41063-020-00079-8
Hossain, A., Knorr, G., Jokat, W., Lohmann, G., Hochmuth, K., Gierz, P. & Gohl, K. (2022): Climate model results of different Miocene and Preindustrial atmospheric CO_2 concentrations experiments of AWI-ESM2 in NetCDF format. [Dataset]. PANGAEA. Retrieved from https://doi.org/10.1594/PANGAEA.943430
Huber, M., & Caballero, R. (2011). The early Eocene equable climate problem revisited. Climate of the Past, 7(2), 603–633. https://doi.org/10.5194/cp-7-603-2011
Kageyama, M., Harrison, S. P., Kapsch, M.-L., Lofverstrom, M., Lora, J. M., Mikolajewicz, U., et al. (2021). The PMIP4 Last Glacial Maximum experiments: preliminary results and comparison with the PMIP3 simulations, Clim. Past, 17, 1065–1089, https://doi.org/10.5194/cp-17-1065-2021.
Kiehl, J. T., & Shields, C. A. (2013). Sensitivity of the Palaeocene-Eocene Thermal Maximum climate to cloud properties. Philosophical Transactions of the Royal Society A: Mathematical, Physical and Engineering Sciences, 371(2001), 20130093.
Knorr, G., Butzin, M., Micheels, A., & Lohmann, G. (2011). A warm Miocene climate at low atmospheric CO2 levels. Geophysical Research Letters, 38(20), L20701. https://doi.org/10.1029/2011GL048873
Knorr, G., & Lohmann, G. (2014). Climate warming during Antarctic ice sheet expansion at the Middle Miocene transition. Nature Geoscience, 7, 376–381. https://doi.org/10.1038/ngeo2119
Krapp, M., & Jungclaus, J. H. (2011). The Middle Miocene climate as modeled in an atmosphere-ocean-biosphere model. Climate of the Past, 7(4), 1169–1188. https://doi.org/10.5194/cp-7-1169-2011
Kürschner, W. M., Kvaček, Z., & Dilcher, D. L. (2008). The impact of Miocene atmospheric carbon dioxide fluctuations on climate and the evolution of terrestrial ecosystems. Proceedings of the National Academy of Sciences of the United States of America, 105, 449–453.

https://doi.org/10.1073/pnas.0708588105
Lawrence, K., Coxall, H., & Sosdian, S., & Steinthorsdottir, M. (2021). Miocene temperature portal. Dataset version 2. Bolin Centre Database. https://doi.org/10.17043/miocene-temperature-portal-2
Lohmann, G. (2020). Temperatures from Energy Balance Models: the effective heat capacity matters. *Earth System Dynamics*, *11*(4), 1195-1208, https://doi.org/10.5194/esd-11-1195-2020.
Lohmann, G., Butzin, M., Eissner, N., Shi, X., & Stepanek, C. (2020). Abrupt climate and weather changes across time scales. *Paleoceanography and Paleoclimatology*, *35*(9), e2019PA003782, https://doi.org/10.1029/2019PA003782.
Lohmann, G., Knorr, G., Hossain, A. & Stepanek, C. (2022). Effects of CO2 and ocean mixing on Miocene and Pliocene temperature gradients, Paleoceanography and Paleoclimatology, 35(7), https://doi.org/10.1029/2020PA003953.
Laîné, A., Yoshimori, M., & Abe-Ouchi, A. (2016). Surface Arctic amplification factors in CMIP5 models: land and oceanic surfaces and seasonality. J. Clim. 29,3297–3316.
Lunt, D. J., Haywood, A. M., Schmidt, G. A., Salzmann, U., Valdes, P. J., Dowsett, H. J., & Loptson, C. A. (2012). On the causes of mid-Pliocene warmth and polar amplification. Earth and Planetary Science Letters, 321–322, 128–138. https://doi.org/10.1016/j.epsl.2011.12.042
Lunt, D. J., Bragg, F., Chan, W.-L., Hutchinson, D. K., Ladant, J.-B., Morozova, P., et al. (2021). DeepMIP: model intercomparison of early Eocene climatic optimum (EECO) large-scale climate features and comparison with proxy data, Clim. Past, 17, 203–227, https://doi.org/10.5194/cp-17-203-2021
Micheels, A., A. A. Bruch, & V. Mosbrugger (2009), Miocene climate modelling sensitivity experiments for different CO2 concentrations, Palaeontol. Electron., 12, 1–20.
Mikolajewicz, U., & Crowley, T. J. (1997). Response of a coupled ocean/energy balance model to restricted flow through the Central American Isthmus. Paleoceanography, 12(3), 429–441. https://doi.org/10.1029/96PA03542
Mitchell, J. F., Senior, C. A., & Ingram, W. J. (1989). C02 and climate: a missing feedback?. *Nature*, *341*(6238), 132-134.
Müller, R. D., Seton, M., Zahirovic, S., Williams, S. E., Matthews, K. J., Wright, N. M., et al. (2016). Ocean Basin evolution and global-scale plate reorganization events since Pangea breakup. Annual Review of Earth and Planetary Sciences, 44(1), 107–138. Doi: 10.1146/annurev-earth-060115-012211
Otto-Bliesner, B. L., Brady, E. C., Zhao, A., Brierley, C. M., Axford, Y., Capron, E., et al. (2021). Large-scale features of Last Interglacial climate: results from evaluating the lig127k simulations for the Coupled Model Intercomparison Project (CMIP6)–Paleoclimate Modeling Intercomparison Project (PMIP4), Clim. Past, 17, 63–94, https://doi.org/10.5194/cp-17-63-2021.
Paxman, G. J. G., Jamieson, S. S. R., Hochmuth, K., Gohl, K., Bentley, M. J., Leitchenkov, G., & Ferraccioli, F. (2019). Reconstructions of Antarctic topography since the Eocene–Oligocene boundary. Palaeogeography, Palaeoclimatology, Palaeoecology 535, 109346.
Pagani, M., Huber, M., Liu, Z., Bohaty, S. M., Henderiks, J., Sijp, W., Krishnan, S., & DeConto, R. M. (2013) The role of carbon dioxide during the onset of Antarctic glaciation. Science 334(6060):1261-4. https://doi.org/10.1126/science.1203909
Raddatz, T. J., Reick, C. H., Knorr, W., Kattge, J., Roeckner, E., Schnur, R., et al. (2007). Will the tropical land biosphere dominate the climate–carbon cycle feedback during the twenty-first century? Climate Dynamics, 29(6), 565–574. https://doi.org/10.1007/s00382-007-0247-8
Rae, J. W., Zhang, Y. G., Liu, X., Foster, G. L., Stoll, H. M., & Whiteford, R. D. (2021). Atmospheric CO2 over the past 66 million years from marine archives. Annual Review of Earth and Planetary Sciences, 49, 609-641.
Royer, D. L. (2001). Stomatal density and stomatal index as indicators of paleoatmospheric CO2 concentration. Review of Palaeobotany and Palynology, 114, 1–28. https://doi.org/10.1016/S0034-6667(00)00074-9
Scholz P., Sidorenko D., Gurses O., Danilov S., Koldunov N., Wang Q., et al. (2019). Assessment of the Finite VolumE Sea Ice Ocean Model (FESOM2.0), Part I: Description of selected key model elements and comparison to its predecessor version. Geoscientific Model Development Discussions. https://doi.org/10.5194/gmd-2018-329, 1–42.
Shevenell, A. E., Kennett, J. P., & Lea, D. W. (2004). Middle Miocene Southern Ocean cooling and

antarctic cryosphere expansion. Science, 305(5691), 1766–1770. https://doi.org/10.1126/science.1100061

Sidorenko, D., Goessling, H. F., Koldunov, N., Scholz, P., Danilov, S., Barbi, D., et al. (2019). Evaluation of FESOM2.0 coupled to ECHAM6.3: Preindustrial and HighResMIP simulations. *Journal of Advances in Modeling Earth Systems*, *11*, pp.3794-3815.

Soden, B. J. & Held, I. M. (2006). An assessment of climate feedbacks in coupled ocean-atmosphere models. J. Clim. 19, 3354–3360.

Sosdian, S. M., Babila, T. L., Greenop, R., Foster, G. L., & Lear, C. H. (2020). Ocean carbon storage across the middle Miocene: A new interpretation for the Monterey event. Nature Communications, 11, 134. https://doi.org/10.1038/s41467-019-13792-0

Sosdian, S. M., Greenop, R., Hain, M. P., Foster, G. L., Pearson, P. N., & Lear, C. H. (2018). Constraining the evolution of Neogene ocean carbonate chemistry using the boron isotope pH proxy. Earth and Planetary Science Letters, 498, 362–376. https://doi.org/10.1016/j.epsl.2018.06.017

Spicer, R. A., Herman, A. B., & Kennedy, E. M. (2004). The foliar physiognomicrecord of climatic conditions during dormancy: CLAMP and the cold monthmean temperature. J. Geol., 112, 685–702. https://doi.org/10.1086/424579

Stärz, M., Jokat, W., Knorr, G., & Lohmann, G. (2017). Threshold in North Atlantic-Arctic Ocean circulation controlled by the subsidence of the Greenland-Scotland Ridge. *Nature communications*, *8*, 15681. https://doi.org/10.1038/ncomms15681

Steckler, M. S., & Watts, A. B. (1978). Subsidence of the Atlantic-type continental margin off New York. *Earth and planetary science letters*, *41*(1), 1-13.

Steele, M., Morley, R., & Ermold, W. (2001). PHC: A global ocean hydrography with a high-quality Arctic Ocean. *Journal of Climate*, *14*(9), 2079-2087, https://doi.org/10.1175/1520-0442(2001)014<2079:PAGOHW>2.0.CO;2.

Stein, U., & Alpert, P. I. N. H. A. S. (1993). Factor separation in numerical simulations. Journal of the Atmospheric Sciences, 50(14), 2107–2115. https://doi.org/10.1175/1520-0469(1993)050<2107:FSINS>2.0.CO;2

Steinthorsdottir, M., Coxall, H. K., De Boer, A. M., Huber, M., Barbolini, N., Bradshaw, C.D., et al. (2021). The Miocene: The future of the past. *Paleoceanography and Paleoclimatology*, *36*(4), p.e2020PA004037.

Stevens, B., Giorgetta, M., Esch, M., Mauritsen, T., Crueger, T., Rast, S. et al. (2013). Atmospheric component of the MPI-M Earth System Model: ECHAM6. Journal of Advances in Modeling Earth Systems, 5, 146–172. https://doi.org/10.1002/jame.20015

Stoll, H. M., Guitian, J., Hernandez-Almeida, I., Mejia, L. M., Phelps, S., Polissar, P., et al. (2019). Upregulation of phytoplankton carbon concentrating mechanisms during low CO2 glacial periods and implications for the phytoplankton pCO2 proxy. *Quaternary Science Reviews*, *208*, 1-20.

Straume, E. O., Gaina, C., Medvedev, S., & Nisancioglu, K. H. (2020). Global Cenozoic Paleobathymetry with a focus on the Northern Hemisphere Oceanic Gateways. *Gondwana Research*.

Super, J. R., Thomas, E., Pagani, M., Huber, M., O'Brien, C., & Hull, P. M. (2018). North Atlantic temperature and pCO2 coupling in the early-middle Miocene. Geology, 46(6), 519–522. https://doi.org/10.1130/G40228.1

Super, J. R., Thomas, E., Pagani, M., Huber, M., O'Brien, C. L., & Hull, P. M. (2020). Miocene Evolution of North Atlantic Sea Surface Temperature. Paleoceanography and Paleoclimatology, 35(5). https://doi.org/10.1029/2019PA003748

Utescher, T., & Mosbrugger, V. (2007). Eocene vegetation patterns reconstructed from plant diversity – A global perspective. Palaeogeography, Palaeoclimatology, Palaeoecology, 247, 243-271. https://doi.org/10.1016/j.palaeo.2006.10.022

Valcke, S. (2013). The OASIS3 coupler: A European climate modelling community software. Geoscientific Model Development, 6(2), 373–388. https://doi.org/10.5194/gmd-6-373-2013

Valdes, P. J., Sellwood, B. W., & Price, G. D. (1996). The concept of Cretaceous equability. Palaeoclim.: Data Model., 1, 139-158.

Von der Heydt, A., & Dijkstra, H. A. (2006). Effect of ocean gateways on the global ocean circulation in the late Oligocene and early Miocene. Paleoceanography, 21, PA1011.

https://doi.org/10.1029/2005PA001149
Vorrath, M.-E., Müller, J., Rebolledo, L., Cárdenas, P., Shi, X., Esper, O., et al. (2020). Sea ice dynamics in the Bransfield Strait, Antarctic Peninsula, during the past 240 years: a multi-proxy intercomparison study, Clim. Past, 16, 2459–2483, https://doi.org/10.5194/cp-16-2459-2020
Zelinka, M. D., Klein, S. A. & Hartmann, D. L. (2012). Computing and partitioning cloud feedbacks using cloud property histograms. Part II: attribution to changes in cloud amount, altitude, and optical depth. J. Clim. 25, 3736–3754.
Zhang, Z., Ramstein, G., Schuster, M., Li, C., Contoux, C., & Yan, Q. (2014). Aridification of the Sahara Desert caused by Tethys Sea shrinkage during the Late Miocene. Nature, 513, 401–404. https://doi.org/10.1038/nature13705
Zhu, J., & Poulsen, C. J. (2019). Quantifying the cloud particle-size feedback in an Earth System Model. Geophysical Research Letters, 46(19), 10910–10917. https://doi.org/10.1029/2019GL083829
Zhu, J., Poulsen, C. J., & Tierney, J. E. (2019). Simulation of Eocene extreme warmth and high climate sensitivity through cloud feedbacks. Science Advances, 5(9), eaax1874. https://doi.org/10.1126/sciadv.aax1874

References from the Supplementary Information

Herbert, T. D., Peterson, L. C., Lawrence, K. T., & Liu, Z. (2010). Tropical ocean temperatures over the past 3.5 million years. Science, 328, 1530–1534. https://doi.org/10.1126/science.1185435
Herbert, T. D., Ng, G., & Cleaveland Peterson, L. (2015). Evolution of Mediterranean Sea surface temperatures 3.5−1.5 Ma: Regional and hemispheric influences. Earth and Planetary Science Letters, 409, 307–318. https://doi.org/10.1016/j.epsl.2014.10.006
Herbert, T. D., Lawrence, K. T., Tzanova, A., Peterson, L. C., Caballero-Gill, R., & Kelly, C. S. (2016). Late Miocene global cooling and the rise of modern ecosystems. Nature Geosciences, 9(11), 843–847. https://doi.org/10.1038/ngeo2813
Herbert, T. D., Rose, R., Dybkjær, K., Rasmussen, E. S., & Śliwińska, K. K. (2020). Bihemispheric warming in the Miocene climatic optimum as seen from the Danish North Sea. *Paleoceanography and Paleoclimatology*, *35*(10), e2020PA003935.
Sosdian, S. M., & Lear, C. H. (2020). Initiation of the western Pacific warm pool at the middle Miocene climate transition?. *Paleoceanography and Paleoclimatology*, *35*(12), e2020PA003920.

Herbert, T. D., Dalton, C. A., Liu, Z., Salazar, A., Si, W., & Wilson, D. S. (2022). Tectonic degassing drove global temperature trends since 20 Ma. *Science*, *377*(6601), 116-119.

Brovkin, V., Raddatz, T., Reick, C. H., Claussen, M., & Gayler, V. (2009). Global biogeophysical interactions between forest and climate. *Geophysical research letters*, *36*(7).

Reick, C. H., Raddatz, T., Brovkin, V., & Gayler, V. (2013). Representation of natural and anthropogenic land cover change in MPI-ESM. *Journal of Advances in Modeling Earth Systems*, *5*(3), 459-482.

Giorgetta, M. A., Jungclaus, J., Reick, C. H., Legutke, S., Bader, J., Böttinger, M., et al. (2013). Climate and carbon cycle changes from 1850 to 2100 in MPI-ESM simulations for the Coupled Model Intercomparison Project phase 5. *Journal of Advances in Modeling Earth Systems*, *5*(3), 572-597.

Groner, V. P., Raddatz, T., Reick, C. H., & Claussen, M. (2018). Plant functional diversity affects climate–vegetation interaction. *Biogeosciences*, *15*(7), 1947-1968.

Lear, C. H., Coxall, H. K., Foster, G. L., Lunt, D. J., Mawbey, E. M., Rosenthal, Y., et al. (2015). Neogene ice volume and ocean temperatures: Insights from infaunal foraminiferal Mg/Ca paleothermometry. *Paleoceanography*, *30*(11), 1437-1454.

Sauermilch, I., Whittaker, J. M., Klocker, A., Munday, D. R., Hochmuth, K., Bijl, P. K., & LaCasce, J. H. (2021). Gateway-driven weakening of ocean gyres leads to Southern Ocean cooling. *Nature communications*, *12*(1), 1-8. https://doi.org/10.1038/s41467-021-26658-1

Ho, S. L., & Laepple, T. (2016). Flat meridional temperature gradient in the early Eocene in the subsurface rather than surface ocean. *Nature Geoscience*, *9*(8), 606-610.

Table 1: *List of sensitivity experiments including relevant model parameters.*

Model Exp.	Greenland-Scotland Ridge depth (m)	max. Fram depth (m)	Bathymetry & topography	atmos. CO_2 (ppm)
MIO_280	~410 m	~2,400 m	Middle Miocene	280
MIO_450	~410 m	~2,400 m	Middle Miocene	450
MIO_720	~410 m	~2,400 m	Middle Miocene	720
PI_CTRL	~1,100 m	~2,800 m	preindustrial	280
PI_450	~1,100 m	~2,800 m	preindustrial	450

Table 2: *Key diagnostics of different model simulations.*

Model Ex.	Mean SAT (ºC)	Mean SST (ºC)	Mean temperature at ~2400 m	Mean SSS (psu)	Mean Arctic SAT (ºC)	DJF mean Arctic SAT (ºC)	MAM mean Arctic SAT (ºC)	JJA mean Arctic SAT (ºC)	SON mean Arctic SAT (ºC)	Mean Arctic SST (ºC)	Mean SSS Arctic (psu)	Equator to pole* temperature gradient (K)	Global mean vert. Integr water vapour (kg/m^2)
MIO_280	14.7	17.5	3.1	34.8	–15.2	–28.7	–18.4	–0.8	–12.5	–1.6	31.7	34.4	22.7
MIO_450	16.4	18.7	3.9	34.7	–9.8	–21.8	–13.8	–0.3	–3.6	–1.4	31.2	31.8	25.5
MIO_720	18.1	20.0	4.7	34.6	–5.1	–10.9	–9.5	0.7	–0.4	–0.7	30.8	29.4	28.9
PI_CTRL	13.3	16.6	1.8	34.6	–16.9	–33.1	–22.3	–1.6	–18.5	–1.8	32.8	34.6	21.4
PI_450	14.7	17.5	3.2	34.7	–12.8	–27.8	–17.4	–1.1	–11.6	–1.6	32.3	32.2	23.6

* Equator-to-pole temperature gradient for proxies is 24.5 ºC

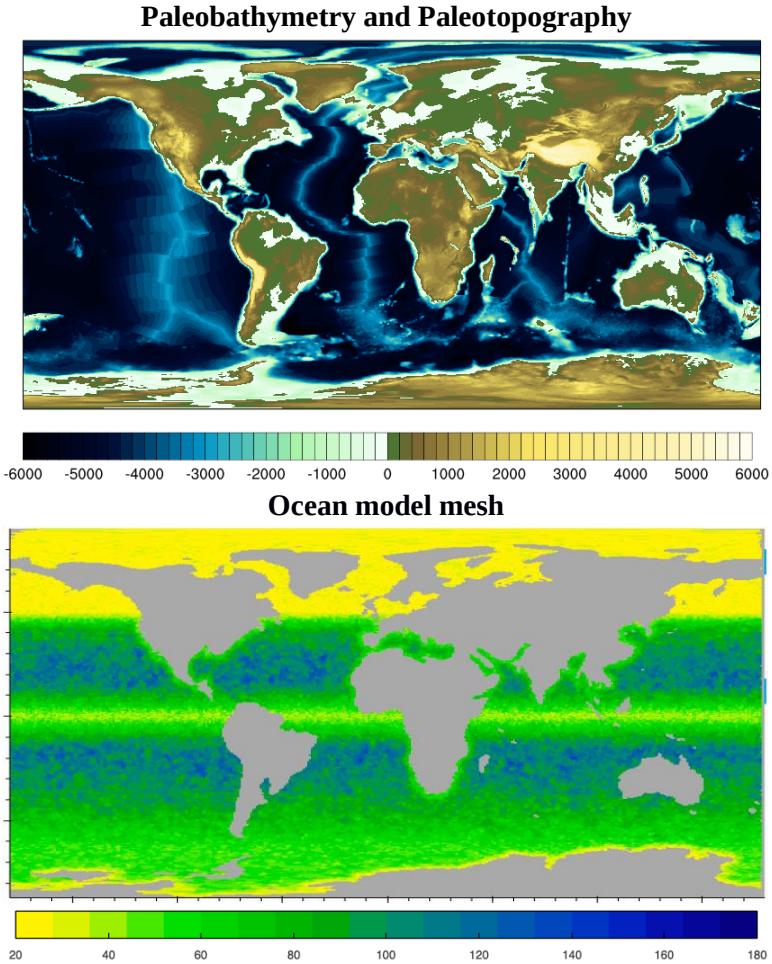

Figure 1: *Global compilation of Middle Miocene paleobathymetry and paleotopography (in m) (Paxman et al., 2019; Hochmuth et al., 2020a; Straume et al., 2020) and the ocean model mesh (in km).*

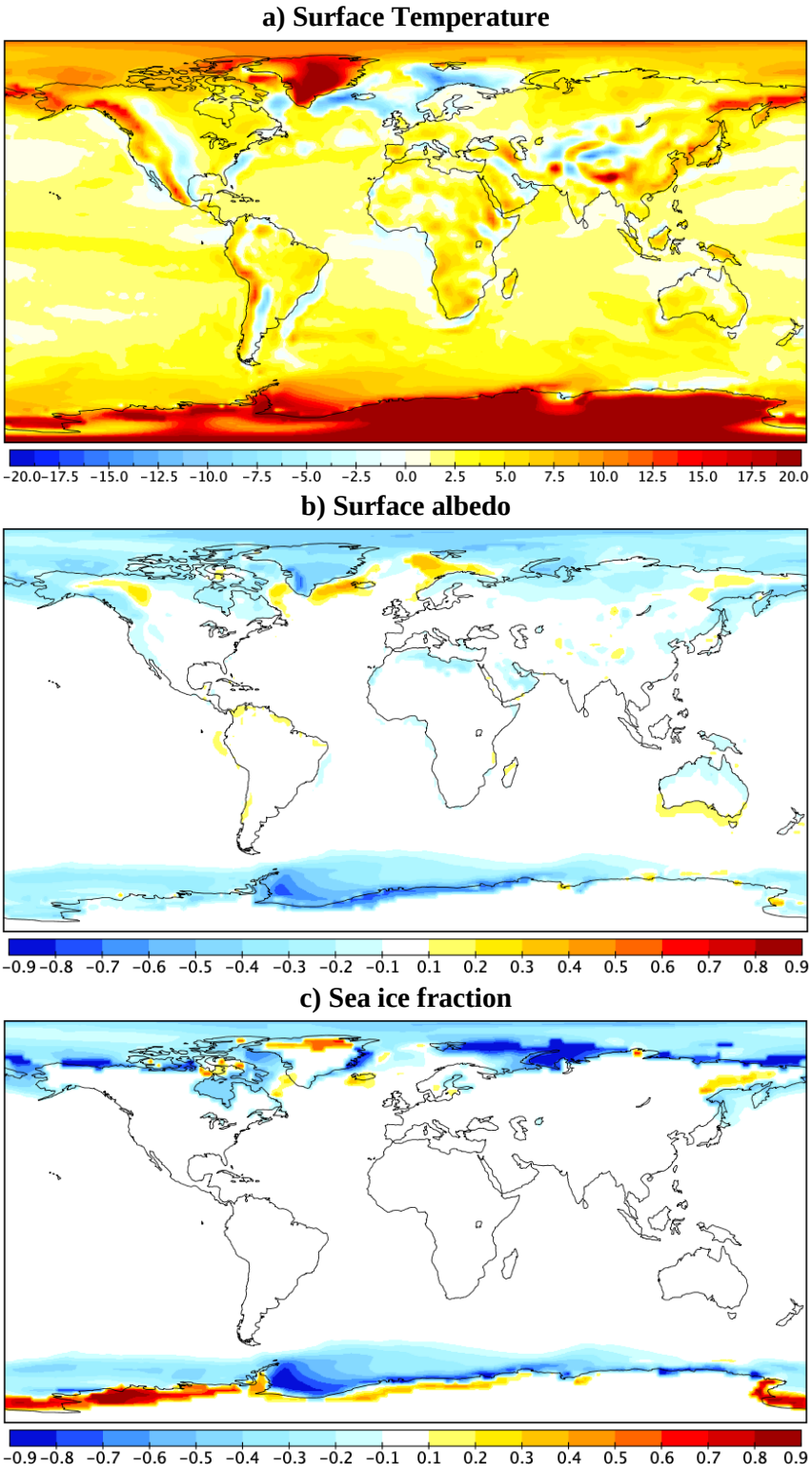

Figure 2. *Annually averaged differences of a) surface air temperature (SAT; in °C), b) surface albedo and c) sea ice fraction between the Middle Miocene (MIO_450) and the pre-industrial climate state (PI_CTRL).*

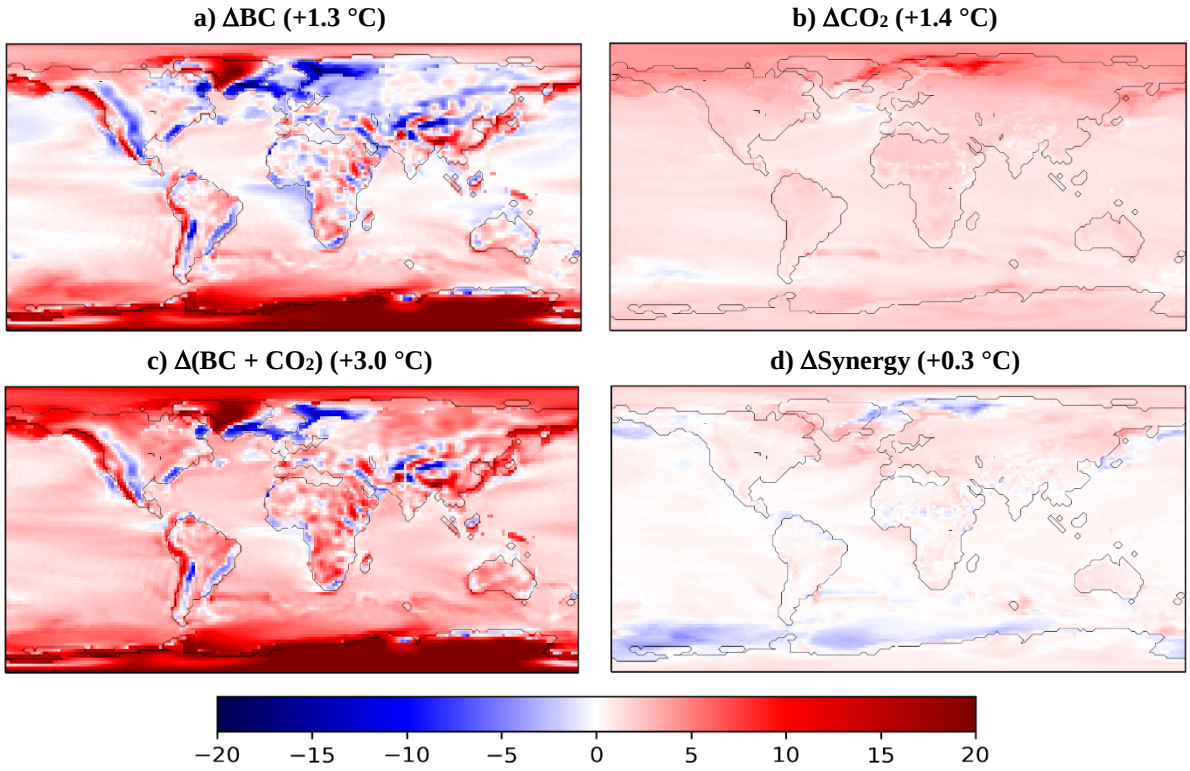

Figure 3. *Application of a synergy analysis between non-CO_2 boundary conditions and atmospheric CO_2. Synergy analysis (ΔSynergy, d) between a) changing non-CO_2 Miocene boundary conditions (ΔBC), b) changing CO_2 (ΔCO_2), and c) the combined effect Δ(BC+CO2) with respect to a change in the surface air temperature (SAT in* °C*).*

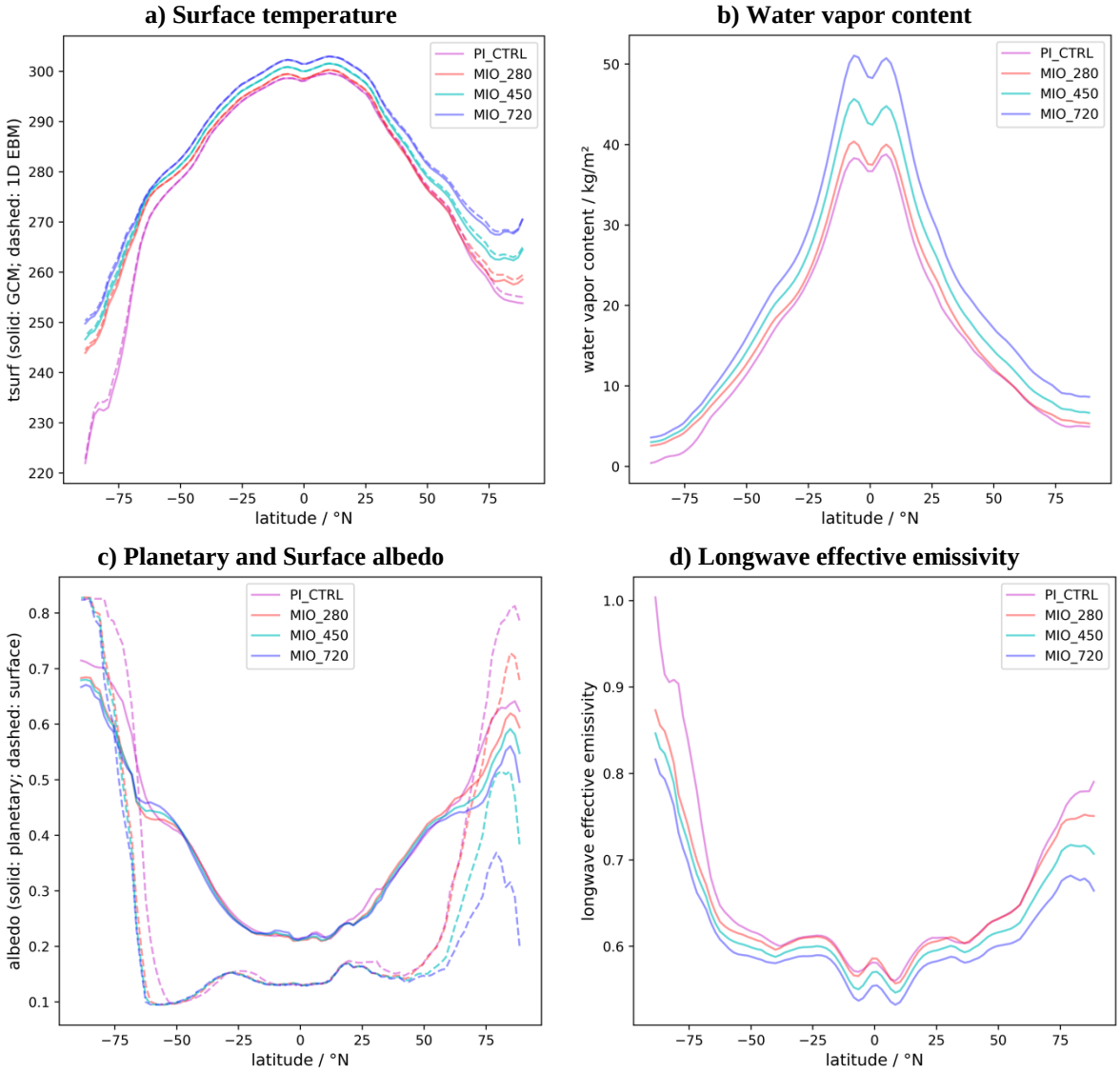

Figure 4. *Meridional profile of contributors to temperature change in Miocene simulations. a) Zonal mean profiles of the Miocene surface temperature (in K) as calculated by climate model (solid lines) and as diagnosed from one-dimensional (1D-EBM) energy balance model (dashed lines); b) vertically integrated water vapor content in the climate model; c) surface albedo, simulated by the climate model (dashed), and planetary albedo, diagnosed from the 1D-EBM (solid); d) effective longwave emissivity diagnosed from the 1D-EBM.*

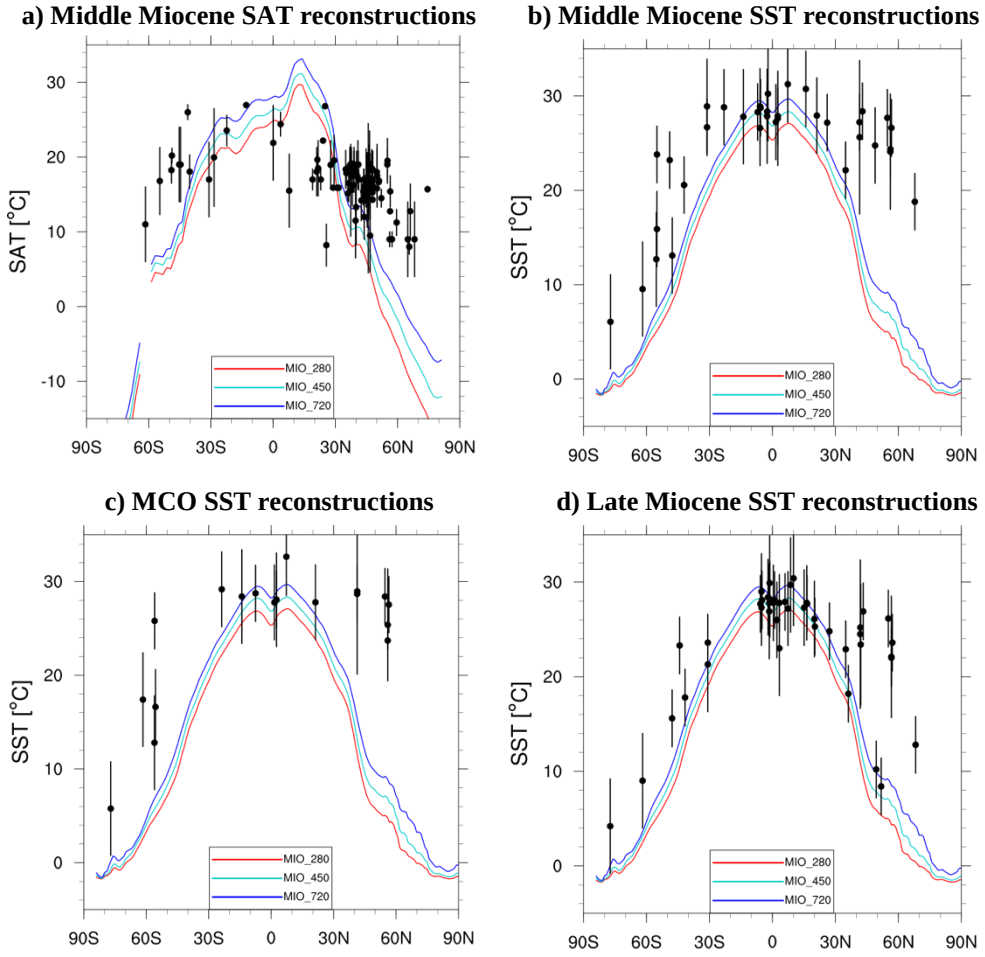

Figure 5. *a) Zonal-annual-mean surface air temperature (SAT; in °C) for all Miocene experiments. The circles localize Middle Miocene terrestrial temperature reconstructions (Burls et al., 2021). Zonal-annual-mean sea air temperature (SST; in °C) for all Miocene experiments are shown in b-d. The circles localize b) Middle Miocene, c) Miocene Climatic Optimum (MCO) and d) Late Miocene SST reconstructions (Table S5).*

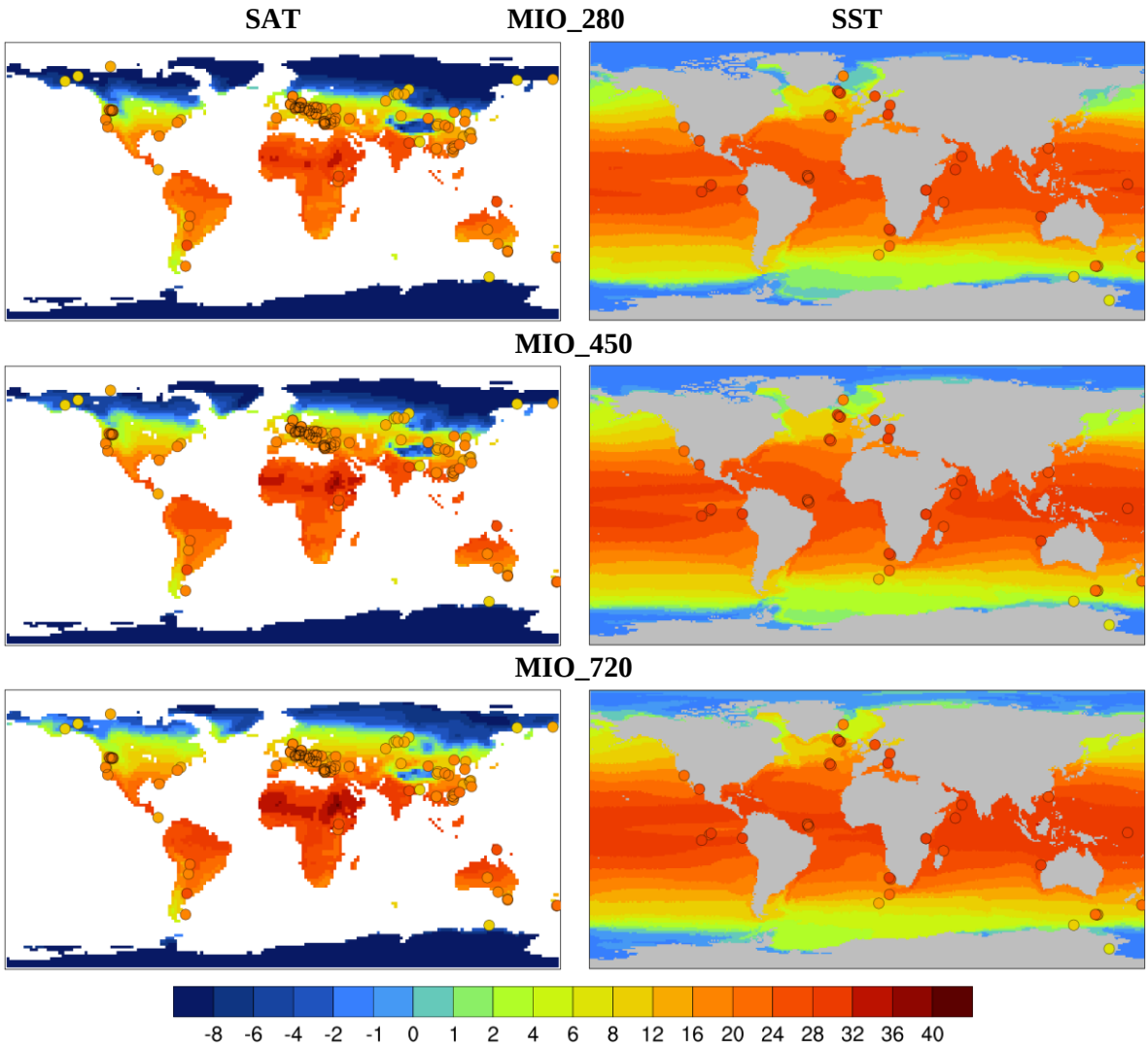

Figure 6. *Global annual mean surface temperature of different Miocene experiments compared with the Middle Miocene mean annual surface air temperature (SAT; in °C) and sea air temperature (SST; in °C) reconstructions. Background color fill: simulated global pattern of annual mean SAT and SST (in °C; left: SAT; right: SST). Colors of circles show the temperature as recorded by different proxy records, respectively.*

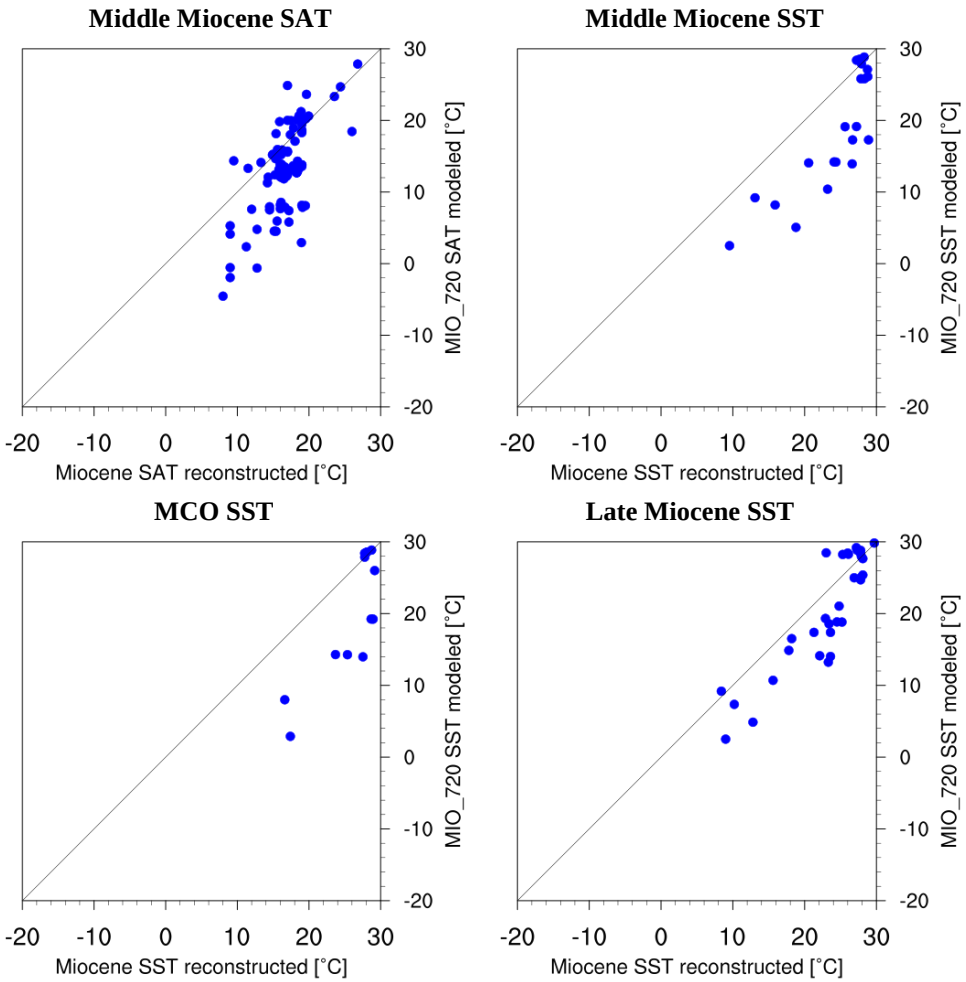

Figure 7. *Model fit: Comparison of reconstructed temperature changes of the annual mean Miocene temperature reconstructions vs. Miocene experiment (that fit best with proxy reconstructions). All other cases are shown in the Supplementary Information (Figure S5). The black line represents the 1:1 slope that indicates a perfect fit between reconstruction and simulation.*

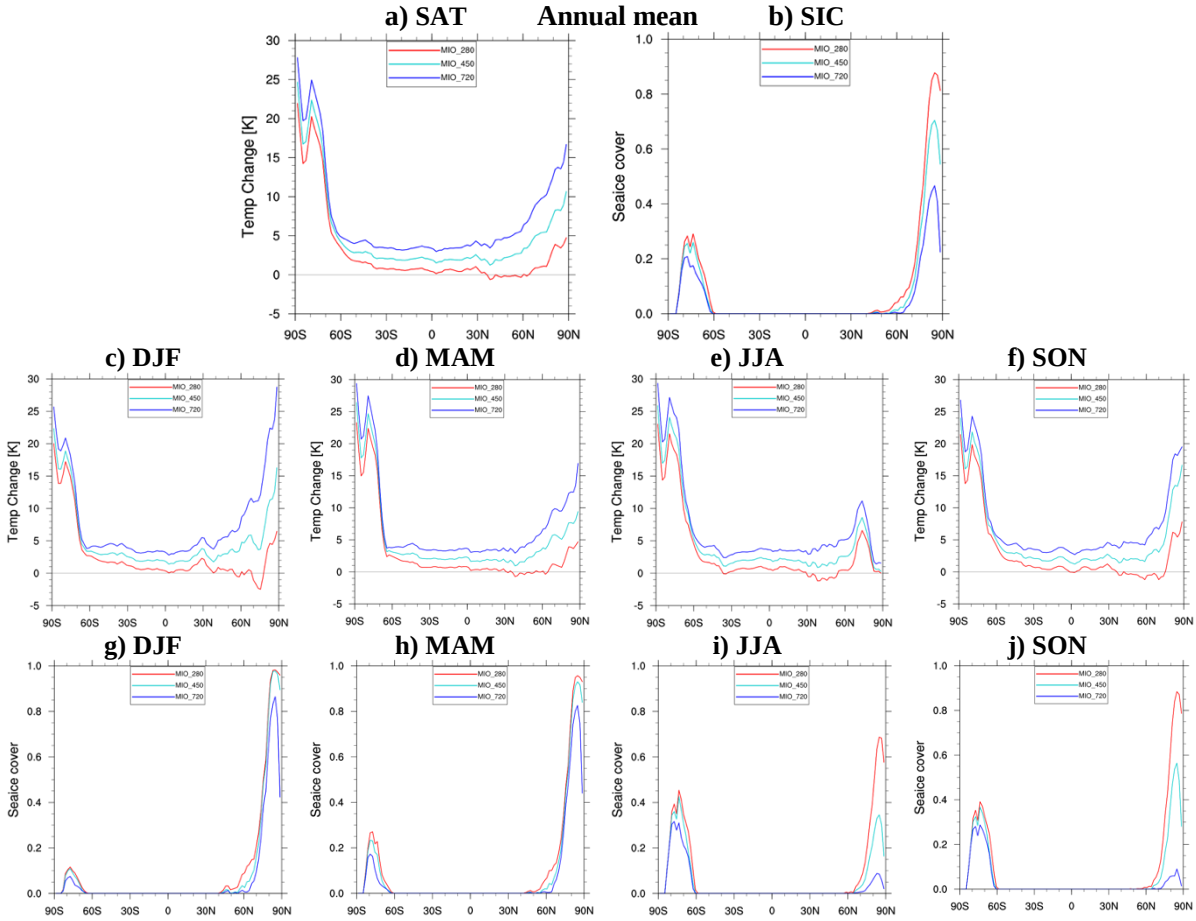

Figure 8. *Zonal means of surface air temperature (SAT) and sea ice cover (SIC). Mean SAT change of Miocene experiments relative to the preindustrial state shown as a) annual mean (upper panel), c) December-January-February (DJF), d) March-April-May (MAM), e) June-July-August (JJA) and f) September-October-November (SON) (middle panel). Zonal mean SIC of Miocene experiments shown as g) annual (top row), g) DJF, h) MAM, i) JJA and j) SON (bottom panel).*

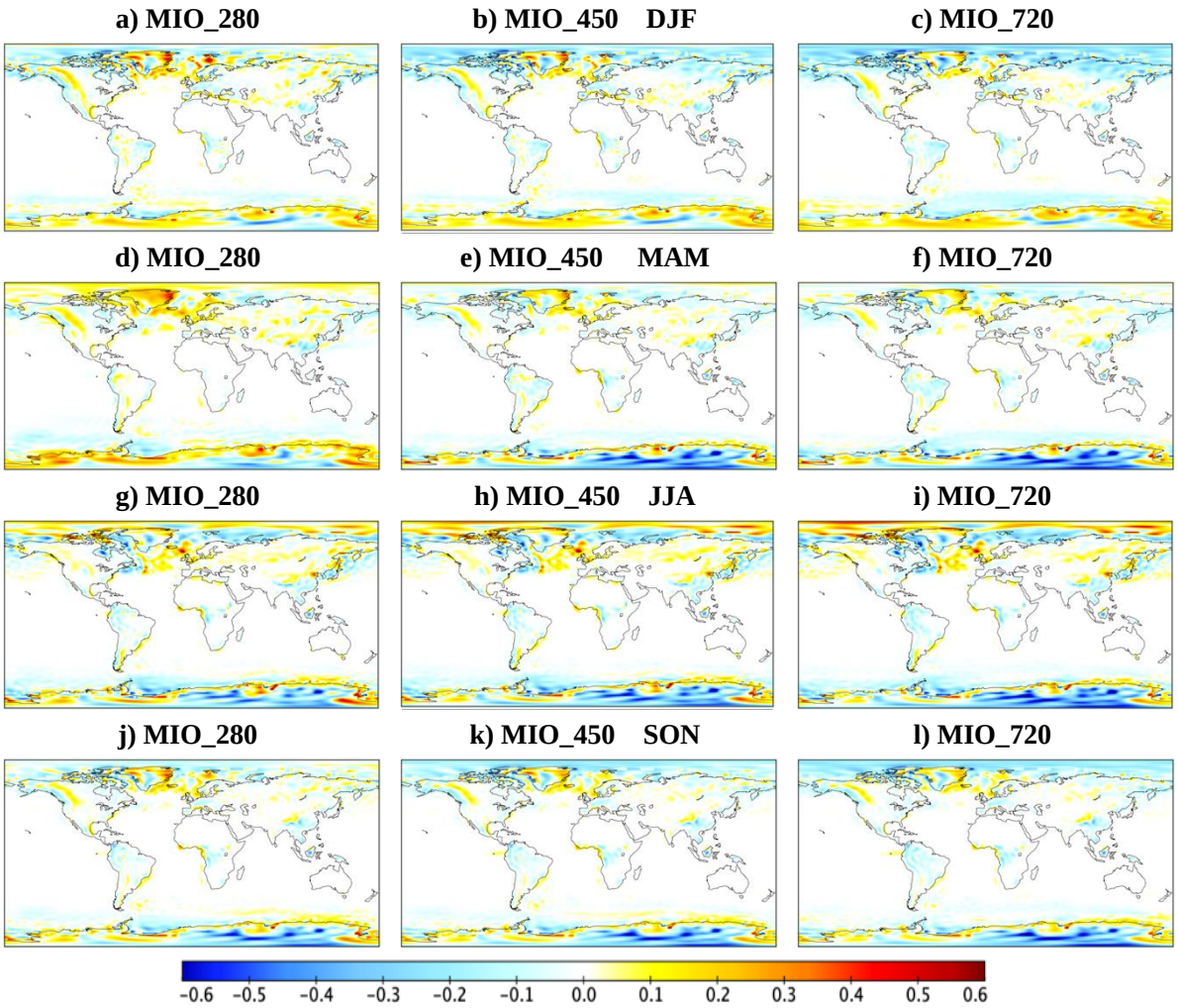

Figure 9. *Global high-level cloud cover change of Middle Miocene experiments relative to the pre-industrial climate states (PI_CTRL) shown for a-c) December-January-February (DJF), d-f) March-April-May (MAM), g-i) June-July-August (JJA) and j-l) September-October-November (SON)*

Miocene sea surface temperature (SST) datasets applied in this study (representing an extended version of the original table published in Burls et al., 2022)

Site	Proxy	Ocean basin	Latitude	Longitude	Modern SST	Depth (m)	Age (Ma)	Avg. Sample Resolution (kyr)	References	Link to Data
594	$U^{k'}_{37}$	Pacific Ocean	46ºS	175ºE	11.1	1204	2.74-12.36	43 kyr (2.8-7.3 Ma); 150 (7.3-12.3 Ma)	Herbert et al. 2016	NOAA - NCDC
608	TEX_{86}; $U^{k'}_{37}$	Atlantic Ocean	43ºN	23ºW	16	3526	8.92-26.68	80	Super et al. 2018	Pangaea
608	TEX_{86}	Atlantic Ocean	43ºN	23ºW	16	3526	0-8.47	207	Super et al. 2020	Pangaea
722	$U^{k'}_{37}$	Indian Ocean	17ºN	60ºE	26.8	2028	0 -10.35	3 kyr (0-3.3 Ma); 103 kyr (3.5-10.35 Ma)	Huang et al. 2007; Herbert et al. 2010	NOAA - NCDC
722	TEX_{86}	Indian Ocean	17ºN	60ºE	26.8	2028	6-13.56	269	Zhuang et al. 2017	Geology
730	TEX_{86}	Indian Ocean	7.7ºN	57.7ºE	27.7	1066	8-14.82	250	Zhuang et al. 2017	Geology
761	Mg/Ca	Indian Ocean	16ºS	115ºE	27.4	2466	11.5-16.5	23	Sosdian et al. 2020	Nature Communications
769	TEX_{86}	Pacific Ocean	9ºN	121ºE	28.5	3643	2.8-11.25	1408	Zhang et al. 2014	Science Magazine
806	Mg/Ca	Pacific Ocean	0ºN	159ºE	29.3	2520	11.3-16.5	100	Sosdian & Lear 2020	Zenodo
806	TEX_{86}	Pacific Ocean	0ºN	159ºE	29.3	2520	0.1-12.01	132	Zhang et al. 2014	Science Magazine
806	Mg/Ca	Pacific Ocean	0ºN	159ºE	29.3	2520	6.5, 7.5 & 8.9 Ma	snapshots	Nathan and Leckie 2009	Pangaea
846	$U^{k'}_{37}$	Pacific Ocean	3ºS	91ºW	23.7	3645	0-12.34	2 kyr (0-5Ma) ; 75 kyr (5-12.34 Ma)	Liu & Herbert 2004; Lawrence et al. 2006; Herbert et al. 2016	NOAA - NCDC
850	$U^{k'}_{37}$; TEX_{86}	Pacific Ocean	1ºN	111ºW	24.9	3796	0-11.88	150	Zhang et al. 2014	Science Magazine
883/884	$U^{k'}_{37}$	Pacific Ocean	51ºN	168ºE	6.5	2384	2.71-11.35	29	Herbert et al. 2016	NOAA - NCDC
887	$U^{k'}_{37}$	Pacific Ocean	54ºN	148ºW	6.8	3647	5.15-7.33	35	Herbert et al. 2016	NOAA - NCDC
907	$U^{k'}_{37}$	Atlantic Ocean	69ºN	13ºW	3.2	1801	2.86-13.08	9	Herbert et al. 2016	NOAA - NCDC
925	Uk'37; TEX_{86}	Atlantic Ocean	4ºN	44ºW	27.4	3042	0-38.62	1997	Zhang et al. 2013	The Royal Society
926	Mg/Ca	Atlantic Ocean	3ºN	42ºW	27.4	3598	0-20.09	224	Sosdian et al. 2018	Pangaea
982	$U^{k'}_{37}$	Atlantic Ocean	58ºN	16ºW	11.6	1134	0 -15.96	4 kyr (0-4Ma); 82 kyr (4-15.96 Ma)	Lawrence et al. 2009; Herbert et al. 2016	NOAA -NCDC
982	$U^{k'}_{37}$; TEX_{86}	Atlantic Ocean	58ºN	16ºW	11.6	1134	0.82-18.38	177	Super et al. 2020	Pangaea
1000	Mg/Ca	Atlantic Ocean	16ºN	79ºW	27.8	927	5.8-8.5	880	Sosdian et al. 2018	Pangaea
1010	$U^{k'}_{37}$	Pacific Ocean	30ºN	118ºW	17.4	3464	0.04-13.53	67	LaRivere et al. 2012	Nature Magazine
1021	$U^{k'}_{37}$	Pacific Ocean	39ºN	128ºW	14.5	4226	0.2-13.11	67	LaRivere et al. 2012	Nature Magazine
1085	$U^{k'}_{37}$; TEX_{86}	Atlantic Ocean	30ºS	14ºE	18.2	1713	0.01-13.67	207	Rommerskirchen et al. 2011	Pangaea
1088	$U^{k'}_{37}$	Atlantic Ocean	41ºS	14ºE	13.2	2082	0.1-12.21	50	Herbert et al. 2016	NOAA - NCDC
1092	Mg/Ca	Atlantic Ocean	46ºS	7ºE	5.9	1974	13.2 - 14.375	19	Kuhnert et al. 2009	Pangaea
1125	$U^{k'}_{37}$	Pacific Ocean	42ºS	178ºW	14.8	1360	0-11.12	62	Herbert et al. 2016	NOAA - NCDC
1143	TEX_{86}	Pacific Ocean	9ºN	113ºE	28.4	2772	0.279-10.85	167	Zhang et al. 2014	Science Magazine
1146	Mg/Ca	Pacific Ocean	19ºN	116ºE	28	2092	6.03-10.1	20	Steinke et al. 2010	Pangaea
1146	Mg/Ca	Pacific Ocean	19ºN	116ºE	28	2092	12.73-15.68	5	Holbourn et al. 2010	Pangaea
1146	Mg/Ca	Pacific Ocean	19ºN	116ºE	28	2092	5.07-8.11	6	Holbourn et al. 2018	Pangaea
1171	TEX86	Southern Ocean	49ºS	149ºE	9.5	2150	11.8-15.5	32	Leutert et al. 2020	Pangaea
1171	Δ47	Southern Ocean	49ºS	149ºE	9.5	2150	11.7-15.4	263	Leutert et al. 2020	Pangaea
1171	Mg/Ca	Southern Ocean	49ºS	149ºE	9.5	2150	12.75-17.03	15	Shevenell et al. 2004	Pangaea
1208	$U^{k'}_{37}$	Pacific Ocean	36.1ºN	158.5ºE	18.2	3346	0-9.78	40	LaRivere et al. 2012	Nature Magazine
1241	$U^{k'}_{37}$; TEX_{86}	Pacific Ocean	6ºN	86ºW	27.4	2027	0-9.54	136	Seki et al. 2012	Pangaea
1406	$U^{k'}_{37}$; TEX_{86}	Atlantic Ocean	40ºN	52ºW	17.3	3814	17.9-29.7	264; **206**	Guitian et al. 2019	Paleoceanography and Paleoclimatology
U1318	TEX86; Uk'37	Atlantic Ocean	51ºN	11.3ºE	12.6	409	12.7-16.6	17	Sangiorgi et al. 2021	Pangaea
U1337	$U^{k'}_{37}$	Pacific Ocean	3.5ºN	123ºW	26.4	4463	0-8	21	Liu et al., 2019	Science Advances - supplement
U1338	Mg/Ca	Pacific Ocean	3ºS	118ºW	25.6	4200	13.3-15.6		Fox et al. 2021	National Geoscience Data Centre
U1338	$U^{k'}_{37}$	Pacific Ocean	3ºS	118ºW	25.6	4200	0.42-16.04	69	Rousselle et al. 2013	NOAA - NCDC
U1338	Mg/Ca	Pacific Ocean	3ºS	118ºW	25.6	4200	5.59-6.37	71	Drury et al. 2018	Pangaea
U1338	Δ47	Pacific Ocean	3ºS	118ºW	25.6	4200	5.05 & 5.99 Ma	snapshots	Drury and John 2016	Pangaea
U1356	TEX_{86}	Southern Ocean	63ºS	136ºE	0	3992	13.41-16.95	236	Sangiogi et al. 2018	Pangaea
AND-A2	TEX_{86}	Southern Ocean	78ºS	165ºE	N/A	N/A	11.51-20.2	505	Levy et al. 2016	Pangaea
LOM-1	Mg/Ca	other	49ºN	25ºE	N/A	N/A	14.35	snapshot	Scheiner et al., 2018	Pangaea

Med	$U^{k'}_{37}$	other	44ºN	14ºE	18	N/A	0-12.92	7	Emeis et al. 2000 & 2003; Tzanova et al. 2015; Herbert et al. 2015; Herbert et al. 2016	NOAA - NCDC
Sdr Vdium	Uk'37	other	55.8ºN	8.4ºW	10	100	8-8-21.8	292	Herbert et al. 2020	Pangaea
Sunbird-1	$\delta^{18}O$ glassy foraminifera	Indian Ocean	4.3ºS	40ºW	27.5	723	9.38-13.68	50	Nairn et al. 2021	Zenodo
Sunbird-1	Mg/Ca	Indian Ocean	4.3ºS	40ºW	27.5	723	9.53-13.23	10-500	Nairn et al. 2021	Zenodo

Miocene sea surface temperature estimates applied in this study (representing an extended version of the original table published in Burls et al., 2022)

Site	Proxy	Age (Ma)	Reference	Modern latitude	Modern longitude	Modern SST (deg C)	Late Miocene SST (deg C)	Late Miocene Uncertainty (deg C)	Late Miocene Lat (ºN)	Late Miocene Lon (ºE)
594	$U^{k'}_{37}$	2.74-12.36	Herbert et al. 2016	46ºS	175ºE	11.1	15.6	3.00	-47.78	179.26
608	TEX_{86}; $U^{k'}_{37}$	8.92-26.68	Super et al. 2018	43ºN	23ºW	16	25.2	3.00	41.89	-23.34
608	TEX_{86}; $U^{k'}_{37}$	8.92-26.68	Super et al. 2018	43ºN	23ºW	16	24.5	7.84	41.87	-23.35
608	TEX_{86}	0-8.47	Super et al. 2020	43ºN	23ºW	16	23.4	6.39	42.09	-23.31
722	$U^{k'}_{37}$	0 -10.35	Huang et al. 2007; Herbert et al. 2010	17ºN	60ºE	26.8	27.7	3.00	16.51	60.82
722	TEX_{86}	6-13.56	Zhuang et al. 2017	17ºN	60ºE	26.8	27.8	3.93	16.37	61.02
730	TEX_{86}	8-14.82	Zhuang et al. 2017	7.7ºN	57.7ºE	27.7	27.2	3.91	7.42	57.35
761	Mg/Ca	11.5-16.5	Sosdian et al. 2020	16ºS	115ºE	27.4	28.4	4.00	-22.08	113.22
769	TEX_{86}	2.8-11.25	Zhang et al. 2014	9ºN	121ºE	28.5	29.7	5.00	8.66	121.00
806	TEX_{86}	0.1-12.01	Zhang et al. 2014	0ºN	159ºE	29.3	29.9	5.00	-1.31	166.41
806	Mg/Ca	6.5, 7.5 & 8.9 Ma	Nathan and Leckie 2009	0ºN	159ºE	29.3	28.2	4.00	-1.20	165.98
846	$U^{k'}_{37}$	0-12.34	Liu & Herbert 2004; Lawrence et al. 2006; Herbert et al. 2016	3ºS	91ºW	23.7	28.1	3.00	-4.93	-83.71
850	TEX86	0-11.88	Zhang et al. 2014	1ºN	111ºW	24.9	26.9	5.00	-1.50	-103.89
850	$U^{k'}_{37}$	0-11.88	Zhang et al. 2014	1ºN	111ºW	24.9	27.8	3.00	-1.50	-103.89
883/884	$U^{k'}_{37}$	2.71-11.35	Herbert et al. 2016	51ºN	168ºE	6.5	10.2	3.00	49.46	173.16
887	$U^{k'}_{37}$	5.15-7.33	Herbert et al. 2016	54ºN	148ºW	6.8	8.4	3.00	51.81	-141.86
907	$U^{k'}_{37}$	2.86-13.08	Herbert et al. 2016	69ºN	13ºW	3.2	12.8	3.00	68.23	-14.73
925	Uk'37	0-38.62	Zhang et al. 2013	4ºN	44ºW	27.4	27.8	3.00	3.31	-41.14
925	TEX_{86}	0-38.62	Zhang et al. 2013	4ºN	44ºW	27.4	23.0	5.00	3.31	-41.14
926	Mg/Ca	0-20.09	Sosdian et al. 2018	3ºN	42ºW	27.4	26.0	4.00	2.16	-39.58
982	$U^{k'}_{37}$	0 -15.96	Lawrence et al. 2009; Herbert et al. 2016	58ºN	16ºW	11.6	23.6	3.00	57.15	-16.92
982	TEX_{86}	0.82-18.38	Super et al. 2020	58ºN	16ºW	11.6	22.1	6.42	56.68	-16.74
982	$U^{k'}_{37}$	0.82-18.38	Super et al. 2020	58ºN	16ºW	11.6	22.0	3.00	56.70	-16.72
1000	Mg/Ca	5.8-8.5	Sosdian et al. 2018	16ºN	79ºW	27.8	27.3	4.00	15.12	-79.52
1010	$U^{k'}_{37}$	0.04-13.53	LaRivere et al. 2012	30ºN	118ºW	17.4	24.8	3.00	27.17	-110.95

1021	$U^{k'}_{37}$	0.2-13.11	LaRivere et al. 2012	39ºN	128ºW	14.5	18.2	3.00	36.19	-121.09
1085	$U^{k'}_{37}$	0.01-13.67	Rommerskirchen et al. 2011	30ºS	14ºE	18.2	23.6	3.00	-30.77	14.21
1085	TEX_{86}	0.01-13.67	Rommerskirchen et al. 2011	30ºS	14ºE	18.2	21.3	5.00	-30.77	14.21
1088	$U^{k'}_{37}$	0.1-12.21	Herbert et al. 2016	41ºS	14ºE	13.2	17.8	3.00	-41.61	14.26
1092	Mg/Ca	13.2 - 14.375	Kuhnert et al. 2009	46ºS	7ºE	5.9				
1125	$U^{k'}_{37}$	0-11.12	Herbert et al. 2016	42ºS	178ºW	14.8	23.3	3.00	-44.20	-172.35
1143	TEX_{86}	0.279-10.85	Zhang et al. 2014	9ºN	113ºE	28.4	30.4	5.00	10.06	114.34
1146	Mg/Ca	6.03-10.1	Steinke et al. 2010	19ºN	116ºE	28	25.3	3.00	20.22	116.86
1146	Mg/Ca	12.73-15.68	Holbourn et al. 2010	19ºN	116ºE	28				
1146	Mg/Ca	5.07-8.11	Holbourn et al. 2018	19ºN	116ºE	28	26.1	4.00	20.02	116.72
1171	TEX86	11.8-15.5	Leutert et al. 2020	49ºS	149ºW	9.5				
1171	Δ47	11.7-15.4	Leutert et al. 2020	49ºS	149ºW	9.5				
1171	Mg/Ca	12.75-17.03	Shevenell et al. 2004	49ºS	149ºW	9.5				
1208	$U^{k'}_{37}$	0-9.78	LaRivere et al. 2012	36.1ºN	158.5ºE	18.2	22.9	3.00	34.94	166.69
1241	$U^{k'}_{37}$; TEX_{86}	0-9.54	Seki et al. 2012	6ºN	86ºW	27.4	27.9	3.00	6.00	-86.00
U1318	TEX86; Uk'37	12.7-16.6	Sangiorgi et al. 2021	51ºN	11.3ºE	12.6				
U1337	$U^{k'}_{37}$	0-8	Liu et al., 2019	3.5ºN	123ºW	26.4	28.1	3.00	1.03	-116.36
U1338	Mg/Ca	13.3-15.6	Fox et al. 2021	3ºS	118ºW	25.6				
U1338	$U^{k'}_{37}$	0.42-16.04	Rousselle et al. 2013	3ºS	118ºW	25.6	27.7	3.00	-5.72	-110.57
U1338	Mg/Ca	5.59-6.37	Drury et al. 2018	3ºS	118ºW	25.6	27.8	4.00	0.45	-112.56
U1356	TEX_{86}	13.41-16.95	Sangiogi et al. 2018	63ºS	136ºE	0	9.0	5.00	-61.84	133.96
AND-A2	TEX_{86}	11.51-20.2	Levy et al. 2016	78ºS	165ºE	N/A	4.2	5.00	-77.26	158.59
LOM-1	Mg/Ca	14.35	Scheiner et al., 2018	49ºN	25ºE	N/A				
Med	$U^{k'}_{37}$	0-12.92	Emeis et al. 2000 & 2003; Tzanova et al. 2015; Herbert et al. 2015; Herbert et al. 2016	44ºN	14ºE	18	26.9	3.00	43.27	13.70
Sdr Vdium	Uk'37	8-8-21.8	Herbert et al. 2020	55.8ºN	8.4ºW	10	26.15	3	55.23	6.24

Miocene sea surface temperature (SST) datasets applied in this study (representing an extended version of the original table published in Burls et al., 2022)

Site	Proxy	Ocean basin	Latitude	Longitude	Modern SST	Depth (m)	Age (Ma)	Avg. Sample Resolution (kyr)	References	Link to Data
594	$U^{k'}_{37}$	Pacific Ocean	46ºS	175ºE	11.1	1204	2.74-12.36	43 kyr (2.8-7.3 Ma); 150 (7.3-12.3 Ma)	Herbert et al. 2016	NOAA - NCDC
608	TEX_{86}; $U^{k'}_{37}$	Atlantic Ocean	43ºN	23ºW	16	3526	8.92-26.68	80	Super et al. 2018	Pangaea
608	TEX_{86}	Atlantic Ocean	43ºN	23ºW	16	3526	0-8.47	207	Super et al. 2020	Pangaea
722	$U^{k'}_{37}$	Indian Ocean	17ºN	60ºE	26.8	2028	0 -10.35	3 kyr (0-3.3 Ma); 103 kyr (3.5-10.35 Ma)	Huang et al. 2007; Herbert et al. 2010	NOAA - NCDC
722	TEX_{86}	Indian Ocean	17ºN	60ºE	26.8	2028	6-13.56	269	Zhuang et al. 2017	Geology
730	TEX_{86}	Indian Ocean	7.7ºN	57.7ºE	27.7	1066	8-14.82	250	Zhuang et al. 2017	Geology
761	Mg/Ca	Indian Ocean	16ºS	115ºE	27.4	2466	11.5-16.5	23	Sosdian et al. 2020	Nature Communications
769	TEX_{86}	Pacific Ocean	9ºN	121ºE	28.5	3643	2.8-11.25	1408	Zhang et al. 2014	Science Magazine
806	Mg/Ca	Pacific Ocean	0ºN	159ºE	29.3	2520	11.3-16.5	100	Sosdian & Lear 2020	Zenodo
806	TEX_{86}	Pacific Ocean	0ºN	159ºE	29.3	2520	0.1-12.01	132	Zhang et al. 2014	Science Magazine
806	Mg/Ca	Pacific Ocean	0ºN	159ºE	29.3	2520	6.5, 7.5 & 8.9 Ma	snapshots	Nathan and Leckie 2009	Pangaea
846	$U^{k'}_{37}$	Pacific Ocean	3ºS	91ºW	23.7	3645	0-12.34	2 kyr (0-5Ma) ; 75 kyr (5-12.34 Ma)	Liu & Herbert 2004; Lawrence et al. 2006; Herbert et al. 2016	NOAA - NCDC
850	$U^{k'}_{37}$; TEX_{86}	Pacific Ocean	1ºN	111ºW	24.9	3796	0-11.88	150	Zhang et al. 2014	Science Magazine
883/884	$U^{k'}_{37}$	Pacific Ocean	51ºN	168ºE	6.5	2384	2.71-11.35	29	Herbert et al. 2016	NOAA - NCDC
887	$U^{k'}_{37}$	Pacific Ocean	54ºN	148ºW	6.8	3647	5.15-7.33	35	Herbert et al. 2016	NOAA - NCDC
907	$U^{k'}_{37}$	Atlantic Ocean	69ºN	13ºW	3.2	1801	2.86-13.08	9	Herbert et al. 2016	NOAA - NCDC
925	Uk'37; TEX_{86}	Atlantic Ocean	4ºN	44ºW	27.4	3042	0-38.62	1997	Zhang et al. 2013	The Royal Society
926	Mg/Ca	Atlantic Ocean	3ºN	42ºW	27.4	3598	0-20.09	224	Sosdian et al. 2018	Pangaea
982	$U^{k'}_{37}$	Atlantic Ocean	58ºN	16ºW	11.6	1134	0 -15.96	4 kyr (0-4Ma); 82 kyr (4-15.96 Ma)	Lawrence et al. 2009; Herbert et al. 2016	NOAA -NCDC
982	$U^{k'}_{37}$; TEX_{86}	Atlantic Ocean	58ºN	16ºW	11.6	1134	0.82-18.38	177	Super et al. 2020	Pangaea
1000	Mg/Ca	Atlantic Ocean	16ºN	79ºW	27.8	927	5.8-8.5	880	Sosdian et al. 2018	Pangaea
1010	$U^{k'}_{37}$	Pacific Ocean	30ºN	118ºW	17.4	3464	0.04-13.53	67	LaRivere et al. 2012	Nature Magazine
1021	$U^{k'}_{37}$	Pacific Ocean	39ºN	128ºW	14.5	4226	0.2-13.11	67	LaRivere et al. 2012	Nature Magazine
1085	$U^{k'}_{37}$; TEX_{86}	Atlantic Ocean	30ºS	14ºE	18.2	1713	0.01-13.67	207	Rommerskirchen et al. 2011	Pangaea
1088	$U^{k'}_{37}$	Atlantic Ocean	41ºS	14ºE	13.2	2082	0.1-12.21	50	Herbert et al. 2016	NOAA - NCDC
1092	Mg/Ca	Atlantic Ocean	46ºS	7ºE	5.9	1974	13.2 - 14.375	19	Kuhnert et al. 2009	Pangaea
1125	$U^{k'}_{37}$	Pacific Ocean	42ºS	178ºW	14.8	1360	0-11.12	62	Herbert et al. 2016	NOAA - NCDC
1143	TEX_{86}	Pacific Ocean	9ºN	113ºE	28.4	2772	0.279-10.85	167	Zhang et al. 2014	Science Magazine
1146	Mg/Ca	Pacific Ocean	19ºN	116ºE	28	2092	6.03-10.1	20	Steinke et al. 2010	Pangaea
1146	Mg/Ca	Pacific Ocean	19ºN	116ºE	28	2092	12.73-15.68	5	Holbourn et al. 2010	Pangaea
1146	Mg/Ca	Pacific Ocean	19ºN	116ºE	28	2092	5.07-8.11	6	Holbourn et al. 2018	Pangaea
1171	TEX86	Southern Ocean	49ºS	149ºE	9.5	2150	11.8-15.5	32	Leutert et al. 2020	Pangaea
1171	Δ47	Southern Ocean	49ºS	149ºE	9.5	2150	11.7-15.4	263	Leutert et al. 2020	Pangaea
1171	Mg/Ca	Southern Ocean	49ºS	149ºE	9.5	2150	12.75-17.03	15	Shevenell et al. 2004	Pangaea
1208	$U^{k'}_{37}$	Pacific Ocean	36.1ºN	158.5ºE	18.2	3346	0-9.78	40	LaRivere et al. 2012	Nature Magazine
1241	$U^{k'}_{37}$; TEX_{86}	Pacific Ocean	6ºN	86ºW	27.4	2027	0-9.54	136	Seki et al. 2012	Pangaea
1406	$U^{k'}_{37}$; TEX_{86}	Atlantic Ocean	40ºN	52ºW	17.3	3814	17.9-29.7	264; **206**	Guitian et al. 2019	Paleoceanography and Paleoclimatology
U1318	TEX86; Uk'37	Atlantic Ocean	51ºN	11.3ºE	12.6	409	12.7-16.6	17	Sangiorgi et al. 2021	Pangaea
U1337	$U^{k'}_{37}$	Pacific Ocean	3.5ºN	123ºW	26.4	4463	0-8	21	Liu et al., 2019	Science Advances - supplement
U1338	Mg/Ca	Pacific Ocean	3ºS	118ºW	25.6	4200	13.3-15.6		Fox et al. 2021	National Geoscience Data Centre
U1338	$U^{k'}_{37}$	Pacific Ocean	3ºS	118ºW	25.6	4200	0.42-16.04	69	Rousselle et al. 2013	NOAA - NCDC
U1338	Mg/Ca	Pacific Ocean	3ºS	118ºW	25.6	4200	5.59-6.37	71	Drury et al. 2018	Pangaea
U1338	Δ47	Pacific Ocean	3ºS	118ºW	25.6	4200	5.05 & 5.99 Ma	snapshots	Drury and John 2016	Pangaea
U1356	TEX_{86}	Southern Ocean	63ºS	136ºE	0	3992	13.41-16.95	236	Sangiogi et al. 2018	Pangaea
AND-A2	TEX_{86}	Southern Ocean	78ºS	165ºE	N/A	N/A	11.51-20.2	505	Levy et al. 2016	Pangaea
LOM-1	Mg/Ca	other	49ºN	25ºE	N/A	N/A	14.35	snapshot	Scheiner et al., 2018	Pangaea

Med	$U^{k'}_{37}$	other	44ºN	14ºE	18	N/A	0-12.92	7	Emeis et al. 2000 & 2003; Tzanova et al. 2015; Herbert et al. 2015; Herbert et al. 2016	NOAA - NCDC
Sdr Vdium	Uk'37	other	55.8ºN	8.4ºW	10	100	8-8-21.8	292	Herbert et al. 2020	Pangaea
Sunbird-1	$\delta^{18}O$ glassy foraminifera	Indian Ocean	4.3ºS	40ºW	27.5	723	9.38-13.68	50	Nairn et al. 2021	Zenodo
Sunbird-1	Mg/Ca	Indian Ocean	4.3ºS	40ºW	27.5	723	9.53-13.23	10-500	Nairn et al. 2021	Zenodo

Miocene sea surface temperature estimates applied in this study (representing an extended version of the original table published in Burls et al., 2022)

Site	Proxy	Age (Ma)	Reference	Modern latitude	Modern longitude	Modern SST (deg C)	Late Miocene SST (deg C)	Late Miocene Uncertainty (deg C)	Late Miocene Lat (ºN)	Late Miocene Lon (ºE)
594	$U^{k'}_{37}$	2.74-12.36	Herbert et al. 2016	46ºS	175ºE	11.1	15.6	3.00	-47.78	179.26
608	TEX_{86}; $U^{k'}_{37}$	8.92-26.68	Super et al. 2018	43ºN	23ºW	16	25.2	3.00	41.89	-23.34
608	TEX_{86}; $U^{k'}_{37}$	8.92-26.68	Super et al. 2018	43ºN	23ºW	16	24.5	7.84	41.87	-23.35
608	TEX_{86}	0-8.47	Super et al. 2020	43ºN	23ºW	16	23.4	6.39	42.09	-23.31
722	$U^{k'}_{37}$	0 -10.35	Huang et al. 2007; Herbert et al. 2010	17ºN	60ºE	26.8	27.7	3.00	16.51	60.82
722	TEX_{86}	6-13.56	Zhuang et al. 2017	17ºN	60ºE	26.8	27.8	3.93	16.37	61.02
730	TEX_{86}	8-14.82	Zhuang et al. 2017	7.7ºN	57.7ºE	27.7	27.2	3.91	7.42	57.35
761	Mg/Ca	11.5-16.5	Sosdian et al. 2020	16ºS	115ºE	27.4	28.4	4.00	-22.08	113.22
769	TEX_{86}	2.8-11.25	Zhang et al. 2014	9ºN	121ºE	28.5	29.7	5.00	8.66	121.00
806	TEX_{86}	0.1-12.01	Zhang et al. 2014	0ºN	159ºE	29.3	29.9	5.00	-1.31	166.41
806	Mg/Ca	6.5, 7.5 & 8.9 Ma	Nathan and Leckie 2009	0ºN	159ºE	29.3	28.2	4.00	-1.20	165.98
846	$U^{k'}_{37}$	0-12.34	Liu & Herbert 2004; Lawrence et al. 2006; Herbert et al. 2016	3ºS	91ºW	23.7	28.1	3.00	-4.93	-83.71
850	TEX86	0-11.88	Zhang et al. 2014	1ºN	111ºW	24.9	26.9	5.00	-1.50	-103.89
850	$U^{k'}_{37}$	0-11.88	Zhang et al. 2014	1ºN	111ºW	24.9	27.8	3.00	-1.50	-103.89
883/884	$U^{k'}_{37}$	2.71-11.35	Herbert et al. 2016	51ºN	168ºE	6.5	10.2	3.00	49.46	173.16
887	$U^{k'}_{37}$	5.15-7.33	Herbert et al. 2016	54ºN	148ºW	6.8	8.4	3.00	51.81	-141.86
907	$U^{k'}_{37}$	2.86-13.08	Herbert et al. 2016	69ºN	13ºW	3.2	12.8	3.00	68.23	-14.73
925	Uk'37	0-38.62	Zhang et al. 2013	4ºN	44ºW	27.4	27.8	3.00	3.31	-41.14
925	TEX_{86}	0-38.62	Zhang et al. 2013	4ºN	44ºW	27.4	23.0	5.00	3.31	-41.14
926	Mg/Ca	0-20.09	Sosdian et al. 2018	3ºN	42ºW	27.4	26.0	4.00	2.16	-39.58
982	$U^{k'}_{37}$	0 -15.96	Lawrence et al. 2009; Herbert et al. 2016	58ºN	16ºW	11.6	23.6	3.00	57.15	-16.92
982	TEX_{86}	0.82-18.38	Super et al. 2020	58ºN	16ºW	11.6	22.1	6.42	56.68	-16.74
982	$U^{k'}_{37}$	0.82-18.38	Super et al. 2020	58ºN	16ºW	11.6	22.0	3.00	56.70	-16.72
1000	Mg/Ca	5.8-8.5	Sosdian et al. 2018	16ºN	79ºW	27.8	27.3	4.00	15.12	-79.52
1010	$U^{k'}_{37}$	0.04-13.53	LaRivere et al. 2012	30ºN	118ºW	17.4	24.8	3.00	27.17	-110.95

1021	$U^{k'}_{37}$	0.2-13.11	LaRivere et al. 2012	39ºN	128ºW	14.5	18.2	3.00	36.19	-121.09
1085	$U^{k'}_{37}$	0.01-13.67	Rommerskirchen et al. 2011	30ºS	14ºE	18.2	23.6	3.00	-30.77	14.21
1085	TEX_{86}	0.01-13.67	Rommerskirchen et al. 2011	30ºS	14ºE	18.2	21.3	5.00	-30.77	14.21
1088	$U^{k'}_{37}$	0.1-12.21	Herbert et al. 2016	41ºS	14ºE	13.2	17.8	3.00	-41.61	14.26
1092	Mg/Ca	13.2 - 14.375	Kuhnert et al. 2009	46ºS	7ºE	5.9				
1125	$U^{k'}_{37}$	0-11.12	Herbert et al. 2016	42ºS	178ºW	14.8	23.3	3.00	-44.20	-172.35
1143	TEX_{86}	0.279-10.85	Zhang et al. 2014	9ºN	113ºE	28.4	30.4	5.00	10.06	114.34
1146	Mg/Ca	6.03-10.1	Steinke et al. 2010	19ºN	116ºE	28	25.3	3.00	20.22	116.86
1146	Mg/Ca	12.73-15.68	Holbourn et al. 2010	19ºN	116ºE	28				
1146	Mg/Ca	5.07-8.11	Holbourn et al. 2018	19ºN	116ºE	28	26.1	4.00	20.02	116.72
1171	TEX86	11.8-15.5	Leutert et al. 2020	49ºS	149ºW	9.5				
1171	Δ47	11.7-15.4	Leutert et al. 2020	49ºS	149ºW	9.5				
1171	Mg/Ca	12.75-17.03	Shevenell et al. 2004	49ºS	149ºW	9.5				
1208	$U^{k'}_{37}$	0-9.78	LaRivere et al. 2012	36.1ºN	158.5ºE	18.2	22.9	3.00	34.94	166.69
1241	$U^{k'}_{37}$; TEX_{86}	0-9.54	Seki et al. 2012	6ºN	86ºW	27.4	27.9	3.00	6.00	-86.00
U1318	TEX86; Uk'37	12.7-16.6	Sangiorgi et al. 2021	51ºN	11.3ºE	12.6				
U1337	$U^{k'}_{37}$	0-8	Liu et al., 2019	3.5ºN	123ºW	26.4	28.1	3.00	1.03	-116.36
U1338	Mg/Ca	13.3-15.6	Fox et al. 2021	3ºS	118ºW	25.6				
U1338	$U^{k'}_{37}$	0.42-16.04	Rousselle et al. 2013	3ºS	118ºW	25.6	27.7	3.00	-5.72	-110.57
U1338	Mg/Ca	5.59-6.37	Drury et al. 2018	3ºS	118ºW	25.6	27.8	4.00	0.45	-112.56
U1356	TEX_{86}	13.41-16.95	Sangiogi et al. 2018	63ºS	136ºE	0	9.0	5.00	-61.84	133.96
AND-A2	TEX_{86}	11.51-20.2	Levy et al. 2016	78ºS	165ºE	N/A	4.2	5.00	-77.26	158.59
LOM-1	Mg/Ca	14.35	Scheiner et al., 2018	49ºN	25ºE	N/A				
Med	$U^{k'}_{37}$	0-12.92	Emeis et al. 2000 & 2003; Tzanova et al. 2015; Herbert et al. 2015; Herbert et al. 2016	44ºN	14ºE	18	26.9	3.00	43.27	13.70
Sdr Vdium	Uk'37	8-8-21.8	Herbert et al. 2020	55.8ºN	8.4ºW	10	26.15	3	55.23	6.24